Wavenumber-dependent transmission of subthreshold waves on electrical synapses network model of *Caenorhabditis elegans*

Iksoo Chang[1, 2, 3], Taegon Chung[1], and Sangyeol Kim[1, 2, *]

[1] Department of Brain Sciences,
[2] Creative Research Initiative Center for Proteome Biophysics,
[3] Supercomputing Bigdata Center,
Daegu Gyeongbuk Institute of Science and Technology, Korea

* Correspondence: Sangyeol Kim, Department of Brain Sciences, Daegu Gyeongbuk Institute of Science and Technology, Korea (sykim@dgist.ac.kr)

Keywords: Electrical synapses network;
Subthreshold oscillations;
Caenorhabditis elegans;
Wavenumber-dependent transmission map;
Synchronized rhythmic activity

Abstract

Recent experimental studies showed that electrically coupled neural networks like in mammalian inferior olive nucleus generate synchronized rhythmic activity by the subthreshold sinusoidal-like oscillations of the membrane voltage. Understanding the basic mechanism and its implication of such phenomena in the nervous system bears fundamental importance and requires preemptively the connectome information of a given nervous system. Inspired by these necessities of developing a theoretical and computational model to this end and, however, in the absence of connectome information for the inferior olive nucleus, here we investigated interference phenomena of the subthreshold oscillations in the reference system *Caenorhabditis elegans* for which the structural anatomical connectome was completely known recently. We evaluated how strongly the sinusoidal wave was transmitted between arbitrary two cells in the model network. The region of cell-pairs that are good at transmitting waves changed according to the wavenumber of the wave, for which we named a wavenumber-dependent transmission map. Also, we unraveled that 1) the transmission of all cell-pairs disappeared beyond a threshold wavenumber, 2) long-distance and regular patterned transmission existed in the body-wall muscles part of the model network, and 3) major hub cell-pairs of the transmission were identified for many wavenumber conditions. A theoretical and computational model presented in this study provided fundamental insight for understanding how the multi-path constructive/destructive interference of the subthreshold oscillations propagating on electrically coupled neural networks could generate wavenumber-dependent synchronized rhythmic activity.

Introduction

The ion current flowing through the gap junction between neurons changes the membrane potential of those neurons, which is called signal transmission by electrical synapses.(Carew and Kandel, 1976) Electrical synapses have characteristics such as simple structure, fast signal transmission, bidirectional communication (in most cases), and a wide operation range for voltage including the subthreshold region.(Bennett, 1997) Based on this, it has been reported that electrical synapses play various roles, such as excitation or inhibition of neurons, synchronization or desynchronization of neural activity, promotion or attenuation of rhythms, and improvement of signal-to-noise ratio, etc.(Connors, 2017) Here, rhythm refers to the periodic active pattern of neurons, and in particular, the rhythm in the subthreshold region helps neurons ignite the action potential simultaneously according to the cycle of the rhythm, and a typical example of this can be seen is the excitatory cells in inferior olivary nucleus.(Bazzigaluppi et al., 2012; Benardo and Foster, 1986; Giocomo et al., 2007; Khosrovani et al., 2007; Long et al., 2002) Spontaneous and robust subthreshold membrane potential oscillations were observed in the inferior olivary cells.(Benardo and Foster, 1986; Chorev et al., 2007; Devor and Yarom, 2002; Lampl and Yarom, 1997; Llinas and Yarom, 1981) The inferior olivary cells are intra-connected only by electrical synapses, and it was reported that the presence of electrical synapses is largely involved in the synchronization of subthreshold oscillations.(De Zeeuw et al., 2003; Leznik and Llinás, 2005; Leznik et al., 2002; Llinás, 2014; Long et al., 2002; Turecek et al., 2016) Although electrical synapses and subthreshold oscillations are functionally closely related, theoretical and computational exploration of this has been lacking. The occurrence of subthreshold oscillations and their role in neural networks have been explored through pioneering neuron models,(Roach et al., 2018; Tchumatchenko and Clopath, 2014; V-Ghaffari et al., 2016) but the establishment of an entire connectome between numerous neurons belonging to regions such as the inferior olivary nucleus remains a task to be solved in the future.

In the field of connectome, information on the indexing of all individual neurons, muscles, and organ cells present in the nematode *Caenorhabditis elegans (C. elegans)* and the entire connectivity between those cells by chemical and electrical synapses was recently updated.(Cook et al., 2019) This available connectome data of *C. elegans* identifies connectivity weights

proportional to the structural size of each synapse, with 1,433 electrical synapses present among a total of 469 cells, including neurons, muscles, pharynx, and other organ cells. Some examples of synchronized activity of a small number of neurons through electrical synapses in *C. elegans* have been reported. During the gentle nose touch response, nose mechanoreceptor neurons connected to electrical synapses simultaneously increased in activity, thereby serving as a coincidence detector.(Chatzigeorgiou and Schafer, 2011) And a pair of GABAergic motor neurons controlling the bowel movement program repeated every 50 seconds used synchronized activity through electrical synapses at their axon terminal.(Choi et al., 2021) However, direct observation or indirect evidence of spontaneous subthreshold oscillations has NOT been confirmed in *C. elegans*. Nevertheless, a theoretical and computational model consideration of the signal transmission of subthreshold oscillations on the entire electrical synapse network among cells with various cell types could be a great challenge.

In general, the wave properties of membrane potential are well-known, such as constructive summation of the two excitatory postsynaptic potentials or deconstructive summation of the excitatory and inhibitory postsynaptic potentials. Likewise, it is experimentally confirmed that subthreshold oscillations have wave properties as fluctuations observed in membrane potential measurements and experience interference when propagated in the neural tissue space.(Chiang and Durand, 2023; Gupta et al., 2016) Therefore, interference should be considered important when subthreshold membrane potential waves propagate through the neural network and cross each other at one spatial point.

Here, we attempted to describe a situation in which wave signals, mimicking the subthreshold membrane potential waves, are propagated and interfered on a network that mimics the electrical synapse network of *C. elegans* (the cells become nodes, the electrical synapses become edges, and the subthreshold waves can flow in both directions on the edges). In the field of physics, the Anderson localization phenomenon has been well known, and it is a general wave phenomenon due to the wave interference between multiple scattering paths. Depending on the strength of the scattering of waves, the result of wave interference could be constructive or destructive, namely, waves could transmit or localize through the media, correspondingly. The theoretical and numerical method for describing the so-called Anderson localization problem usually employed the tight-binding Anderson Hamiltonian. A relevant model was developed to calculate the wave's quantum percolation using the tight-binding Anderson Hamiltonian on a network lattice consisting

of nodes and edges, where the interference by all possible propagation paths was considered when the quantum mechanical probability wave was propagated by experiencing the percolation disorder on the network lattice.(Anderson, 1958; Chang et al., 1995; Meir et al., 1989; Shapir et al., 1982; Thomas and Nakanishi, 2016) In this study, we benefited from this model, and by treating the probability wave as a general wave signal and replacing the network lattice with a synapse network model we are interested in. We could calculate the interference by all possible paths which were considered when the wave signals propagate in the synapse network.

By applying the theoretical concept and computational methodology introduced above and well established in the field of physics, we calculated the signal transmission coefficient between arbitrary two cells of the model connectome as a function of the wavenumber (the quantity of inverse of wavelength) of the wave signal. Based on the signal transmission coefficients for all cell-pairs estimated under various wavenumber conditions, we unraveled 1) the existence of a threshold wavenumber above which the signal transmission disappears, 2) regions of cell-pairs with wavenumber-dependent transmission map, 3) long-distance and regular patterned signal transmission, and 4) major hub cell-pair common across multiple wavenumbers. When comparing with the results for a situation that didn't consider the wave interference, we revealed the role of the interference when subthreshold waves propagate on the *C. elegans'* electrical synapse network model. Although many aspects of the actual neural network and electrical synapses were simplified or omitted in our model study, our results provided the insight of the fundamental role of the electrical synapse network with subthreshold oscillations.

Results

Cell-pairs in the model connectome of *C. elegans* could belong to regions where the wave signal could be transmitted (or not transmitted) below (or above) a threshold wavenumber.

In our circuit model mimicking the anatomical gap junction network of *C. elegans* (details described in "Construction of our circuit model" part of Methods) (Fig. 1), we calculated all the transmission coefficient T_{ij} of the wave signal for each of the 109,746 cell-pairs $\langle i, j \rangle$ between the total 469 cells (details described in "Calculation for the transmission coefficient" part of

Methods). Here, the transmission coefficient was a function of energy E of the incoming wave, and the E value was a function of the wavenumber k of the wave signal. And according to the wavenumber, E value was set up to exist in the range [-10, 10], and we calculated all the $T_{ij}(E)$ of the entire cell-pairs at E values of 801 points listed by equal intervals over the entire range ($\Delta E = 0.025$).

First, the average transmission coefficient of all cell-pairs $\langle i, j \rangle$ for each E value, $\langle T_{ij}(E) \rangle_{All\ ij\ cell-pairs}$, was obtained and drawn as a function of E (Fig. 2A). The $\langle T(E) \rangle$ graph showed an incomplete but quite symmetrical form based on $E = 0$. And on the real Y-axis scale, high $\langle T(E) \rangle$ values were broadly identified in these three ranges of the E values: [-1.575, -1.275], [-0.350, 0.350], and [1.275, 1.575], Also on the log Y-axis scale, several relatively high $\langle T(E) \rangle$ values were locally identified in the form of peaks in the remaining ranges of the E values. Meanwhile, on the log Y-axis scale, the signal transmission of all cell-pairs almost disappeared in the E value range at both ends. In the field of solid-state physics, a threshold energy value in which electrical conductivity disappears in the energy band is called a "mobility edge". We were able to define a threshold wavenumber, namely a signal mobility edge, even in the transmission of the wave signal of our circuit model. For example, considering that $\langle T(E) \rangle = 10^{-7}$ is a value that can be obtained when only one cell-pair out of all cell-pairs shows 1% transmission and all others are completely unable to transmit the wave, this 10^{-7} value can be regarded as an extreme disappearance of signal transmission throughout the entire circuit. Thus, by taking this reference value, $E = \pm 5.650$ in our circuit model became a signal mobility edge. If the reference value is set more conservatively lower than now, the absolute value of E corresponding to the signal mobility edges will be larger than now.

Next, the transmission coefficient of all individual cell-pairs $T_{ij}(E = 0.225)$ was represented as a heatmap at the E value (or the corresponding wavenumber) where the $\langle T(E = 0.225) \rangle$ value was the highest (Fig. 2B). Here, we confirmed that not all cell-pairs transmit the wave signals with even transmission coefficients. Most of the strong transmissions were found in the cell-pairs of intra-body-wall muscles, and a small number of cells belonging to sensory neurons, motor neurons, and other organ cells also showed strong transmission in cell-pairs between them or to body-wall muscles. The rest of the cells except these cells were almost isolated separately without exchanging the wave signals with any cells even at this E value, which

was the highest transmitted state on average.

In addition, the transmission coefficient of all individual cell-pairs $T_{ij}(E = 5.650)$ was represented as a heatmap at the E value (or the corresponding wavenumber) which we defined as the signal mobility edge (Fig. 2C). As expected, all cells were isolated separately without exchanging the wave signals with each other, and the entire circuit stop transmitting wave signals of this wavenumber.

Transmission map of subthreshold waves on the electrical synapse network model depended on values of wavenumber.

Between the two E values discussed above ($E = 0.225$ and $E = 5.650$), the average transmission coefficient of all cell-pairs, $\langle T(E) \rangle$, did not simply increase or decrease, but fluctuated along the E value (Fig. 2). Therefore, it was expected that the composition of the cell-pairs, which showed strong transmission, also changes according to the E value. To efficiently investigate the changes in the composition of the cell-pairs, instead of inspecting the $T_{ij}(E)$ heatmaps in all E values, we selected 31 specific E values and tried to analyze the composition of the cell-pairs only in these E values. We chose the specific E values on the following three criteria: (1) the $\langle T(E) \rangle$ value was the local maximum (the shape of a peak) in the $\langle T(E) \rangle$ graph, (2) the components of the $T_{ij}(E)$ showed greater than 0.5 at least one cell-pair, (3) The E value was positive number (Fig. S1). The reasons why we used these conditions are as follows (1) we assumed that the peak occurred in the $\langle T(E) \rangle$ graph due to the emergence of new cell-pairs with strong transmission, (2) we set the reference value for strong transmission to be 0.5 or higher, and (3) the E values where peak occurred in the $\langle T(E) \rangle$ graph showed left-right symmetry based on $E = 0$. (Additional explanations are in "Auxiliary paragraph 1" of Supplementary Materials.)

The transmission coefficients of all individual cell-pairs were represented as a heatmap at each E value (or the corresponding wavenumber) for the 31 specific E values we selected (Left panels in Fig. 3 and S2-9). To closely observe the composition of cell-pairs with strong transmission, only cells (Table S1-3) belonging to the cell-pairs with $T_{ij}(E) > 0.5$ were selectively exhibited in these heatmaps, not for all 469 cells. To confirm the spatial status of the cell-pairs with strong transmission on the electrical synapse network model, a network diagram was prepared first. Since drawing all 469 cells as a network diagram was complicated and poorly

visible, we presented nodes for only 173 cells that belonged to the cell-pairs with $T_{ij}(E) > 0.5$ in the positive E values. Electrical synapses between cells were represented as edges, and the thickness of the edge proportional to our processed weights (w_{ij}) was used. (Additional explanations are in "Auxiliary paragraph 2" of Supplementary Materials.) On the prepared network diagram, we marked the cell-pairs with strong transmission that satisfies $T_{ij} > 0.5$ (Right panels in Fig. 3 and S2-9).

As expected above, the region of the cell-pairs with strong transmission changed depending on the value of E (or wavenumber), which we named "Wavenumber-Dependent Transmission Map (WDTM) of subthreshold waves on the electrical synapse network model". However, it should be also noted that our WDTM was a result derived from a network where only electrical synapses were considered, not a general neural network where chemical and electrical synapses coexist.

We looked at the cell type of the cell-pairs that make up the 31 WDTMs (Fig. 3 and S2-9). In the two E value ranges of [0, 0.350] and [1.275, 1.575], the high $\langle T(E) \rangle$ value was broadly identified (Fig. S1), and many cell-pairs of intra-body-wall muscles were observed in the corresponding WDTMs of these E values (Fig. 3A, 3C, S2, S3A-B, and S5). Since the body-wall muscles consist of four muscle strands: dorsal/ventral-left/right strands, the cell-pair of intra-body-wall muscles can be divided into two cases: a cell-pair of intra-strand and a cell-pair of inter-strand. Following this classification, the cell-pairs of both intra-strand and inter-strand were found in the WDTMs of the E value range of [0, 0.350] (Fig. 3A, S2, and S3A-B), whereas only the cell-pairs of intra-strand were found in the WDTMs in the E value range of [1.275, 1.575] (Fig. 3C and S5). On the other hand, in the remaining WDTMs, a small number of cell-pairs within cells with less than ten members were mostly found (Fig. 3B, 3D, S3C-D, S4, and S6-9), and the WDTMs of the two largest cases were shown in Fig. 3B and 3D. The composition of cell-pairs with various combinations of cell types (sensory/inter/motor neurons, body-wall/sex-specific muscles, pharynx, and other organ cells) was shown in these remaining WDTMs.

Cell-pairs in body-wall muscles on long-distance with regular patterned transmission were found in the WDTMs.

When looking at each WDTM on the network diagram, it shows various patterns spatially. In particular, in the case of the body-wall muscles, the cell-pairs of intra-strand existed, ranging from

short-distance to the longer distance than the half of the full length of the strand (Fig. 3A and 3C). Here, the "Distance" was meant by the length of the shortest path along the network between two cells of a cell-pair. If two cells are directly connected to an edge, the distance between the two cells is one. In the WDTMs of the E value range of [1.275, 1.575], cell-pairs with regular patterned transmission of the body-wall muscles were observed through the network diagram (Fig. S5). Only the cell-pairs of intra-strand were found in these WDTMs, and the configuration of the distance of these cell-pairs was different for each WDTM (multiple of 3 at $E = 1.350$, multiple of 2 at $E = 1.450$, multiple of 7 at $E = 1.500$, and multiple of 4 at $E = 1.575$).

On the other hand, when the cell-pairs of inter-strand of the body-wall muscles appeared in the WDTMs as shown in Fig. 3A-B, the head mesodermal cell (hmc) seemed to play an important role in building a bridge between them. This would be recognized from the network diagram itself of black edges without WDTM, and hmc was strongly connected near the neck of the body-wall muscles (seventh and eighth muscles) for all four strands. In the WDTM of Fig. 3A, there were many cell-pairs of inter-strand between dorsal-right and ventral-left strands, and there were also many cell-pairs between the ventral-left strand and hmc, which directly revealed the role of hmc as a bridge between the two body-wall muscle strands. In the WDTM of Fig. 3B, it was shown that the role of hmc was indirectly revealed as the cell-pairs of inter-strand, which existed only among the neck of four body-wall muscle strands.

Additionally, we reaffirmed the important role of hmc while confirming the distance characteristics of the cell-pairs with strong transmission. Under the conditions used when preparing the network diagram (the transmission coefficient $T_{ij}(E)$ of a cell-pair was 0.5 or higher in the range of positive E values at least once), a total of 146 cell-pairs with strong transmission were identified excluding the cell-pairs of intra-body-wall muscles, and their distance was investigated (Table S4). (Additional explanations are in “Auxiliary paragraph 3” of Supplementary Materials.) Most of the cell-pairs in Table S4 showed the kinds of short-distances 1 to 3, which consisted of various cell types. On the other hand, the cell-pairs with long-distances in Table S4 ranging from 4 to 17 were mainly pairs between hmc and body-wall muscles. The strong transmission between hmc and the tail muscle, which corresponds to the longest distance, passes through the intra-strand connections from the neck to the tail of body-wall muscles.

A few cell-pairs of strong transmission with long-distance in Table S4 turned out to be not

those between hmc and the body-wall muscles. In there, one inter neuron (AVBR) and two motor neurons (AS11, VD04) formed a cell-pair with the body-wall muscles, respectively, and four sensory neurons (CEPDL, IL1R, IL1DR, OLQDL) formed cell-pairs between them.

Major hub cell-pairs with the strong transmission of signals for many wavenumbers exist.

We looked at cell-pairs frequently appearing in all 31 WDTMs in order to identify the major hub cell-pairs that is commonly used for various wavenumbers. First, for each cell-pair $\langle i, j \rangle$, we calculated the average appearance rate in all 31 WDTMs, $\langle \Theta[T_{ij}(E) - 0.5] \rangle_{E \in \{31\ selected\ E\}}$, and represented this as a heatmap (Fig. 4). Where, the $\Theta[x]$ was a step function, which value was 1 if $x \geq 0$ or 0 if $x < 0$. Thus, the average appearance rate was 1 in the case of a cell-pair that appeared in all 31 WDTMs, and $1/31 \approx 0.03$ in the case of a cell-pair that appeared only once. In this study, we declared a cell-pair as a major hub cell-pair if the average appearance rate of a cell-pair was $3/31 \approx 0.1$ or higher. The major hub cell-pairs were the cell-pairs of intra-strand of the body-wall muscles (Fig. 4). As seen in the network diagram, the edges of each strand of the body-wall muscles from the neck (seventh or eighth muscle) to the tail (twenty-third or twenty-fourth muscle) were simply connected in a line, unlike the messy edges among most neurons in the network (Fig. 3). In general, the complexity of connections among most neurons increase with the number of transmissible paths of wave propagation, and the sum of phase changes coming from various path-length differences causes the deconstructive interference. Therefore, the simple (or regular) connections in each strand of the body-wall muscles from the neck to the tail reduced the number of transmissible paths of wave signals, which suppressed deconstructive interference and thus resulted in the strong transmission for various wavenumbers.

Also, the cell-pairs between hmc and the neck of the ventral-left strand of the body-wall muscles were also identified as major hub cell-pair (Fig. 4). As seen in the network diagram, since the edges between hmc and the neck muscles were very strong compared to other edges (Fig. 3), the relative contribution of wave signals coming from other cells could be almost ignored, and thus resulted in the strong transmission for various wavenumbers.

The cell-pairs among two sensory neurons (PVDL, PVDR) and three other organ cells (CANL, CANR, exc_cell) were also identified as major hub cell-pairs (Fig. 4). The cell-pair between CANL and CANR was the most major hub cell-pair, with the highest average appearance rate of $7/31 \approx$

0.23. As seen in the network diagram, the three other organ cells were very strongly connected by the edges to each other, and the two sensory neurons were very strongly connected by the edges to both ALA inter neuron and hmc (Fig. 3). Although there were cases where they were strongly connected by the edges to each other, such as between PVDL and CANL or between PVDR and CANR, they were not major hub cell-pair. Therefore, the strong edge shown on the network diagram was not a sufficient condition to implicate a major hub cell-pair.

Discussion

The fundamental aspect of this study is that the interference phenomena of the subthreshold oscillations propagating on a neuronal circuit was described by a theoretical and computational model study of the reference system *C. elegans* for which the structural anatomical connectome was completely known. We investigated the wavenumber-dependent transmission of the sinusoidal wave signals between all cell-pairs on the connectome model of *C. elegans* by considering the interference effect caused by multi-paths of signaling.

The results related to the wavenumber-dependent transmission map expanded the way we used to view signal transmission on electrical synapses. The difference in signal transmission with the presence or absence of interference effect on electrical synapses could be illustrated by considering the effective conductance between two nodes in the electric circuit with or without considering the interference effect (Fig. 5). For a situation without considering the interference, we calculated the effective resistance and effective conductance for all cell-pairs by imitating a cell as a node and the electrical synapse as an electrical resistor connecting nodes as shown in Fig. 5A (details in “Calculation for effective conductance” part of Methods). Several inter neurons and other organ cells showed high effective conductance, while pharynx, body-wall muscles from the neck to the tail, and sex-specific muscles showed very low effective conductance (Fig. 5B). Since inter neurons have many complex connections among them, many electrical current paths exist between the two inter neurons, which act as parallel connections of multiple electrical resistors. This results in lower effective resistance (or higher effective conductance). However, for a situation with considering the interference, many transmissible forward and backward paths of the

signal propagation rather caused the deconstructive interference, preventing the transmission of the signal. For each cell-pair $\langle i, j \rangle$, we calculated the average transmission coefficient for all E values and represented this as a heatmap (Fig. 5C-D). Which clearly showed that most of the neurons could not exchange wave signals with each other except for very few neurons. Wave signals were effectively delivered only within a small number of very strongly connected cell groups (PVDL/R, CANL/R, exc_cell, hmc) or within a large number of very regularly connected cell groups (body-wall muscle strands from the neck to the tail).

In this study, we used the structural anatomical information from *C. elegans'* electrical synapse network, but no synchronized rhythmic activity induced by subthreshold membrane potential oscillations has been reported for *C. elegans* so far. However, we aimed at investigating the signaling characteristics caused by the interference and to discover a feasible phenomenon related to the propagation of the subthreshold oscillations on a neuronal circuit of living nervous system. As to the synchronized rhythmic activation observed like in the mammalian inferior olive nucleus, we think that there might be an electrical synapse network in there that connect cells very strongly or very regularly. The plausible possibility according to our model study is that the constructive interference of subthreshold membrane potential waves with a specific wavenumber may generate the synchronized rhythmic activation. We hope that the results in our study would serve as the worthwhile framework and knowledge for designing the future experimental studies not only for inferior olive nucleus, *C. elegans* but also other living systems.

Methods

Construction of our circuit model

We used the contents of the "hermaphrodite gap jn symmetric" tab in the "SI 5 Connectome adjacency matrices, corrected July 2020.xlsx" file of the *C. elegans* connectome dataset as data for the anatomical gap junction network.(Cook et al., 2019) The 469 cell names and the gap junction weight (g_{ij}) of all cell-pairs connected by gap junction were provided in the tab, and the weights had a value distribution from a minimum of 1 to a maximum of 401 (Fig. 1A). The weights were proportional to the spatial size of the corresponding gap junction, which we hypothesized that the

larger the weight, the stronger the connection between the cells and thus the better transmit the wave signal to the connected cell.

Our circuit model described *C. elegans'* anatomical gap junction network as follows (Fig. 1B). First, each cell was treated as a node in our circuit. Each gap junction connected to a cell-pair was treated as an edge connecting two nodes in our circuit, and we inserted two virtual nodes (VNs) between those two nodes to be connected sequentially through VNs (Cell-VN-VN-Cell). Here, all edges inside our circuit were set to have the identical length a. The edge of Cell-to-VN (or VN-to-Cell) representing like axon or dendrite of neuron gave a weight of 1, and the edge of VN-to-VN representing a gap junction gave our processed weight ($w_{ij} = \min\{1, g_{ij}/40\}$). Our processed weight (w_{ij}) was proportional to the anatomical gap junction weight (g_{ij}) and normalized as a value between 0 and 1 but was fixed to 1 if $g_{ij} > 40$. In our circuit model, the weight of the edge meant the transmission coefficient of the signal transmitted through this edge, so if the weight was 1 corresponded to complete transmission, and 0 corresponded to complete reflection (or unavailable edge), respectively. And within our circuit, the characteristic of the signal being spontaneously attenuated, and disappearing was excluded. Therefore, when a signal incoming from the outside to a node in our circuit was reflected to the outside at the same node and simultaneously transmitted to the outside at another node, the sum of the transmission and reflection coefficients to the outside always remained at 1 without loss.

Calculation for the transmission coefficient

We benefited from the method of calculating the transmission coefficient according to the energy E of the incoming wave when the electron probability wave incident on one point of the network lattice was detected on another point. This methodology, called the quantum percolation model, considered the propagation and interference of waves on the network lattice using the tight-binding Anderson Hamiltonian.(Anderson, 1958; Chang et al., 1995; Meir et al., 1989; Shapir et al., 1982; Thomas and Nakanishi, 2016) In our methodology, we replaced the classical wave signals of complex number expression representing subthreshold membrane potential waves instead of the electron probability wave and replaced the network lattice with our circuit describing the electrical synapse network model built above. Then, the transmission coefficient calculated by the quantum percolation model told how well the subthreshold waves were transmitted from one

cell *i* to another cell *j* while undergoing interference by multiple propagation paths in the electrical synapse network model. Here, the electrical synapses act as wave scatters that interrupt the propagation of the subthreshold waves from cell *i* to cell *j*.

In the quantum percolation model, the tight-binding Anderson Hamiltonian was defined as follows,

$$\boldsymbol{H} = \sum_{m} \epsilon_m |m\rangle\langle m| + \sum_{\langle mn \rangle} V_{mn}(|m\rangle\langle n| + |n\rangle\langle m|).$$

Where the $|m\rangle$ (also expressed as the ψ_m) is as the electron probability wave on the *m*-th node, and the $\langle m|$ means its complex conjugate ψ_m^*. We used ψ_m as the classical wave signal observed on the *m*-th node, which of complex number expression made it easy to express the phase shift of the wave and calculate the interference. The amplitude of this classical wave signal on the *m*-th node was defined as the $\langle m|m\rangle = \psi_m^* \psi_m$. In the Hamiltonian, the ϵ_m is the on-site energy, and we regarded it as the resting membrane potential of the *m*-th cell and set it to 0, the identical value as the relative reference value of the resting membrane potential in all cells. The $\langle mn \rangle$ represents a pair of nearest-neighbor sites in the Hamiltonian, we replaced it with a node-pair connected by the edges in our circuit. The V_{mn} as a hopping matrix represents the entire structure of the network lattice in the Hamiltonian, which we implemented the structure of our circuit by setting it to $V_{mn} = 1$ for a node-pair between cell and VN, and $V_{mn} = w_{mn}$ for that between two VNs. Since the total number of the cells was 469, and we inserted two VNs for every 1,433 electrical synapses, the newly constructed tight-binding Anderson Hamiltonian for our circuit was represented as a matrix of 3,335 by 3,335.

By solving the time-independent Schrödinger equation ($\boldsymbol{H}\vec{\psi} = E\vec{\psi}$) for the Hamiltonian of our circuit, we sought to obtain the reflection and transmission coefficients of the cell-pair between the IN-cell and the OUT-cell from the ψ_{IN} of the IN-cell where the wave signal from the outside was incident and reflect, and the ψ_{OUT} of the OUT-cell where the wave signal from our circuit transmitted to the outside. We defined ψ_{IN} and ψ_{OUT} as follows using complex numbers *r* and *t* with amplitudes and phases,

$$\psi_{IN} = 1 + r, \qquad \psi_{OUT} = t.$$

Where the ψ_{IN} was the sum of 1 and *r* corresponding to the incoming wave and the reflective wave, respectively, and the ψ_{OUT} was *t* corresponding to the transmitted wave. The reason why

the amplitude and the phase of the incoming wave on the IN-cell were 1 and 0, respectively was because we set that as a reference amplitude and a reference phase in our circuit. The amplitude of the wave reflected from the IN-cell to the outside became the reflection coefficient with $R = r^{*}r$, and the amplitude of the wave transmitted from the OUT-cell to the outside became the transmission coefficient with $T = t^{*}t$, and $T + R = 1$ had to be always satisfied, as mentioned above.

This methodology also assumed both an external injector and an external detector. The external injector injected the generated wave into the network lattice and received the reflective wave from the network lattice. The external detector received the transmitted wave from the network lattice. The waves on the external injector $\phi_{Injector}$ and the external detector $\phi_{Detector}$ were extended from the definitions of ψ_{IN} and ψ_{OUT} above, respectively, and determined as follows,

$$\phi_{Injector} = 1e^{-ika} + re^{ika}, \qquad \phi_{Detector} = te^{ika}.$$

The external injector and detector were set to be connected to the IN-cell and OUT-cell by a perfect conducting wire with a length of a, respectively. The wave outgoing to the external injector (detector) from the IN-cell (OUT-cell) was determined by multiplying the phase difference of e^{ika} to the wave on the IN-cell (OUT-cell), whereas the wave incoming to the IN-cell from the external injector was determined by multiplying the phase difference of e^{-ika} to the wave on the IN-cell. Insert these terms into the time-independent Schrödinger equation for the Hamiltonian of our circuit, the following equation was derived describing the entire system consisting of our circuit and the external injector and detector,

$$\boldsymbol{H}\psi_m + \phi_{Injector}\delta_{m,IN} + \phi_{Detector}\delta_{m,OUT} = E\psi_m.$$

Where the E value on the right side representing the energy of the entire system was equivalent to the energy E of the incoming wave from the external injector.

In the quantum percolation model, the energy E of the incoming wave was defined as a tight-binding energy function as follows,

$$E = 2\gamma\cos(ka).$$

Where γ meant the binding energy between the nearest-neighbor atoms in the tight-binding model, but we had to set it to an arbitrary value. In this study, it was set to $\gamma = 5$, and the decision process was described in the below section. Applying this energy function, the above equation for

the entire system was expressed as the matrices as follows,

$$\begin{pmatrix} e^{ika} - 2\gamma\cos(ka) & V_{IN,m} & V_{IN,OUT} \\ V_{n,IN} & V_{nm} - 2\gamma\cos(ka)\delta_{nm} & V_{n,OUT} \\ V_{OUT,IN} & V_{OUT,m} & e^{ika} - 2\gamma\cos(ka) \end{pmatrix} \begin{pmatrix} 1 + r \\ \psi_m \\ t \end{pmatrix} = \begin{pmatrix} e^{ika} - e^{-ika} \\ 0 \\ 0 \end{pmatrix}.$$

Where *m* and *n* meant the 3,333 remaining nodes except two nodes for IN-cell and OUT-cell. For a wavenumber *k* in the range of $[0, \pi/a]$ (or an *E* value in the range of $[-2\gamma, 2\gamma]$), all components of both the left-hand square-matrix and the right-hand column-vector were fully expressed as complex numbers, and then the *r* and *t* values in the left-hand column-vector were obtained by matrix multiplication of the inverse matrix of the left-hand square-matrix and the right-hand column-vector. From squared absolute the *r* and *t* values, the reflection and transmission coefficients of the cell-pair between IN-cell and OUT-cell at the *E* value (or the corresponding wavenumber *k*) were deduced, respectively.

Searching for optimal gamma

To determine the appropriate γ of the above energy function, we preliminarily calculated the transmission coefficient for all cell-pairs between the 469 cells under all four conditions of γ, and compared the average transmission coefficient graph as a function of the *E* value $\langle T_{ij}(E)\rangle_{All\ ij\ cell-pairs}$ (Fig. S10). Where four values of 1, 2.5, 5, and 10 were attempted for γ, and equally spaced a hundred values were used for the wavenumber *k* in the range of $[0, \pi/a]$. According to the above energy function, the minimum/maximum range of the *E* value differed as $[-2\gamma, 2\gamma]$, and as γ was larger, the points of the $\langle T(E)\rangle$ graph were placed sparsely on the X-axis of the *E* value. In each of the $\langle T(E)\rangle$ graphs for these four conditions of γ, similarly high $\langle T(E)\rangle$ values occurred in the vicinity of $E = 0, \pm 1.4$. Based on this preliminarily estimation, we confirmed that the occurrence of high $\langle T(E)\rangle$ values appeared as a function of the *E* value regardless of γ. Therefore, we considered γ as just determining the minimum/maximum range of the *E* value.

The appropriate γ we wanted in this study was large enough to provide a wide *E* value range to check the signal mobility edge in the $\langle T(E)\rangle$ graph, and the appropriate γ had to be small so that the points in the $\langle T(E)\rangle$ graph did not become too sparse. It was the condition of $\gamma = 5$ that satisfied this demand out of the four conditions of γ. Because the condition of $\gamma = 2.5$ was not sufficient to confirm the signal mobility edge, and the condition of $\gamma = 10$ had too sparse points

along the X-axis.

Error report on our calculation for the transmission coefficient

In principle, the sum of transmission coefficient $T_{ij}(E)$ and reflection coefficient $R_{ij}(E)$ of any cell-pair at any E value always had to satisfy 1 because our circuit model did not consider spontaneous attenuation of the wave signal. However, in the calculating program we wrote and used for this study, the error occurred with the sum of the two coefficients exceeding 1 (by the tolerance was 10^{-5}) for a total of 5,213 cell-pairs in three specific E values (45 cell-pairs at $E = -1.000$, 3,836 cell-pairs at $E = -0.375$, and 1,332 cell-pairs at $E = 1.000$). We performed the calculations on a total of 109,746 cell-pairs for a total of 801 E values, so these errors correspond to 0.006% of the total calculation results. To eliminate the effect of these errors in this study, we post-corrected the two coefficients of the 5,213 cell-pairs in the three specific E values in which the error occurred to $T_{ij}(E) = 0, R_{ij}(E) = 1$.

Calculation for effective conductance

An electrical resistor network model was constructed that mimics *C. elegans'* electrical synapse network, with the 469 cells replaced with electrical conducting nodes and the 1,433 electrical synapses replaced with electrical resistors connecting these nodes. The effective resistance and its reciprocal, the effective conductance, when a direct current power source outside the electrical resistor network model contacted a cell by its positive pole, and another cell by its negative pole, respectively, were calculated.(Klein and Randic, 1993) The effective conductance shows how well electric current without interference flows between the two cells contacted to the external power source.

We expressed the electric voltage at node i as ν_i, the electric current flowing from node i to node j as μ_{ij}, the resistance of the electrical resistor between node i and node j as χ_{ij}, the conductance of that as ω_{ij} $(= \chi_{ij}^{-1})$. The anatomical gap junction weights (g_{ij}) were used as the conductance value of the electrical resistors in the network, $\omega_{ij} = g_{ij}$, with arbitrary units.

By Ohm's law, each electrical resistor in the network satisfies the following equation,

$$\mu_{ij} = \chi_{ij}^{-1}(\nu_i - \nu_j) = \omega_{ij}(\nu_i - \nu_j).$$

The sum of the electric currents entering each node by Kirchhoff's current law satisfied the

equation below,

$$\sum_{j\neq i}\mu_{ij} = \begin{cases} I, & at\ i = (+) \\ -I, & at\ i = (-). \\ 0, & \text{otherwise} \end{cases}$$

Where $(+)$ and $(-)$ meant a node in which the positive and negative poles of the external power source were in contact, respectively, and the capital letter I was the total electric current supplied by the external power source. When Ohm's law above was substituted on the left-hand of this equation, it was expressed as $\nu_i \sum_{j\neq i}\omega_{ij} - \sum_{j\neq i}\omega_{ij}\nu_j$, and then the equation was able to express in matrix and vector as follows,

$$\boldsymbol{L}^{\omega}\vec{\nu} = I\left(\overrightarrow{e_{(+)}} - \overrightarrow{e_{(-)}}\right).$$

Where $\boldsymbol{L}^{\omega}$ was the Laplacian matrix of the electrical resistors' conductance matrix ($\boldsymbol{\omega}$), defined as $L^{\omega}_{ij} = \delta_{ij}\sum_{\ell}\omega_{i\ell} - \omega_{ij}$, $\vec{\nu}$ was a column-vector with an electric voltage at all nodes as a component, and $\overrightarrow{e_{(+)}}$ ($\overrightarrow{e_{(-)}}$) was a unit column-vector of the identical dimension as $\vec{\nu}$, with only the component of the $(+)$ node ($(-)$ node) having a value of 1 and all other components having a value of 0. By applying the pseudo-inverse matrix of the Laplacian matrix ($\boldsymbol{L}^{\omega+}$) on both sides of the equation, we obtained a particular solution as $\vec{\nu} = I\boldsymbol{L}^{\omega+}\left(\overrightarrow{e_{(+)}} - \overrightarrow{e_{(-)}}\right)$.

The effective resistance applied between the positive and negative poles of the external power source was defined by Ohm's law of the electric voltage difference between the $(+)$ and $(-)$ nodes and the total electric current, as follows,

$$R^{\text{eff}} = I^{-1}\left(\nu_{(+)} - \nu_{(-)}\right) = I^{-1}\left(\overrightarrow{e_{(+)}} - \overrightarrow{e_{(-)}}\right)^{T}\vec{\nu}.$$

Substituting here the particular solution of $\vec{\nu}$ obtained above was as follows,

$$R^{\text{eff}} = \left(\overrightarrow{e_{(+)}} - \overrightarrow{e_{(-)}}\right)^{T}\boldsymbol{L}^{\omega+}\left(\overrightarrow{e_{(+)}} - \overrightarrow{e_{(-)}}\right).$$

As a result, we were able to obtain the effective resistance for any one cell-pair by calculating the pseudo-inverse matrix of the Laplacian matrix ($\boldsymbol{L}^{\omega+}$) from the electrical resistors' conductance matrix ($\boldsymbol{\omega}$). The effective conductance was defined as the reciprocal of the effective resistance, $G^{\text{eff}} = (R^{\text{eff}})^{-1}$.

Acknowledgements

We appreciate two Nobel Laureates, Prof. Erwin Neher and Prof. Kurt Wuthrich, for their insightful discussions on the impact of this work. We have benefited a lot from their suggestions in the course of this study.

Funding

This work was supported in part by both pCoE program of DGIST [grant number: 23-CoE-BT-01] and a grant from iPT, Korea.

Author contributions

IC and SK conceived the idea for this work. TC, IC, and SK set up the model, conducted the calculation, and analyzed the data and results. IC and SK wrote the manuscript. All authors reviewed and agreed on the contents of the manuscript.

Declaration of interests

The authors declare no competing interests.

Data and materials availability

All data are available in the manuscript or the supplementary materials.

References

Anderson, P.W. (1958). Absence of Diffusion in Certain Random Lattices. Phys Rev *109*, 1492-1505.

Bazzigaluppi, P., De Gruijl, J.R., van der Giessen, R.S., Khosrovani, S., De Zeeuw, C.I., and de Jeu, M.T.G. (2012). Olivary subthreshold oscillations and burst activity revisited. Front Neural Circuit *6*.

Benardo, L.S., and Foster, R.E. (1986). Oscillatory Behavior in Inferior Olive Neurons - Mechanism, Modulation, Cell Aggregates. Brain Res Bull *17*, 773-784.

Bennett, M.V.L. (1997). Gap junctions as electrical synapses. J Neurocytol *26*, 349-366.

Carew, T.J., and Kandel, E.R. (1976). Two functional effects of decreased conductance EPSP's: synaptic augmentation and increased electrotonic coupling. Science *192*, 150-153.

Chang, I.S., Lev, Z., Harris, A.B., Adler, J., and Aharony, A. (1995). Localization Length Exponent in Quantum Percolation. Phys Rev Lett *74*, 2094-2097.

Chatzigeorgiou, M., and Schafer, W.R. (2011). Lateral Facilitation between Primary Mechanosensory Neurons Controls Nose Touch Perception in *C. elegans*. Neuron *70*, 299-309.

Chiang, C.C., and Durand, D.M. (2023). Subthreshold Oscillating Waves in Neural Tissue Propagate by Volume Conduction and Generate Interference. Brain Sci *13*.

Choi, U., Wang, H., Hu, M.X., Kim, S., and Sieburth, D. (2021). Presynaptic coupling by electrical synapses coordinates a rhythmic behavior by synchronizing the activities of a neuron pair. P Natl Acad Sci USA *118*.

Chorev, E., Yarom, Y., and Lampl, I. (2007). Rhythmic episodes of subthreshold membrane potential oscillations in the rat inferior olive nuclei. J Neurosci *27*, 5043-5052.

Connors, B.W. (2017). Synchrony and so Much More: Diverse Roles for Electrical Synapses in Neural Circuits. Dev Neurobiol *77*, 610-624.

Cook, S.J., Jarrell, T.A., Brittin, C.A., Wang, Y., Bloniarz, A.E., Yakovlev, M.A., Nguyen, K.C.Q., Tang, L.T.H., Bayer, E.A., Duerr, J.S.*, et al.* (2019). Whole-animal connectomes of both *Caenorhabditis elegans* sexes. Nature *571*, 63-+.

De Zeeuw, C.I., Chorev, E., Devor, A., Manor, Y., Van der Giessen, R.S., De Jeu, M.T., Hoogenraad, C.C., Bijman, J., Ruigrok, T.J.H., French, P.*, et al.* (2003). Deformation of network connectivity in the inferior olive of connexin 36-deficient mice is compensated by morphological and electrophysiological changes at the single neuron level. J Neurosci *23*, 4700-4711.

Devor, A., and Yarom, Y. (2002). Generation and propagation of subthreshold waves in a network of inferior olivary neurons. J Neurophysiol *87*, 3059-3069.

Giocomo, L.M., Zilli, E.A., Fransén, E., and Hasselmo, M.E. (2007). Temporal frequency of subthreshold oscillations scales with entorhinal grid cell field spacing. Science *315*, 1719-1722.

Gupta, N., Singh, S.S., and Stopfer, M. (2016). Oscillatory integration windows in neurons. Nat Commun *7*.

Khosrovani, S., Van der Giessen, R.S., De Zeeuw, C.I., and De Jeu, M.T.G. (2007). mouse inferior olive neurons exhibit heterogeneous subthreshold oscillations and spiking patterns. P Natl Acad Sci USA *104*,

15911-15916.
Klein, D.J., and Randic, M. (1993). Resistance Distance. J Math Chem *12*, 81-95.
Lampl, I., and Yarom, Y. (1997). Subthreshold oscillations and resonant behavior: Two manifestations of the same mechanism. Neuroscience *78*, 325-341.
Leznik, E., and Llinás, R. (2005). Role of gap junctions in synchronized neuronal oscillations in the inferior olive. J Neurophysiol *94*, 2447-2456.
Leznik, E., Makarenko, V., and Llinás, R. (2002). Electrotonically mediated oscillatory patterns in neuronal ensembles:: An *In vitro* voltage-dependent dye-imaging study in the inferior olive. J Neurosci *22*, 2804-2815.
Llinás, R.R. (2014). The olivo-cerebellar system: a key to understanding the functional significance of intrinsic oscillatory brain properties. Front Neural Circuit *7*.
Llinas, R., and Yarom, Y. (1981). Properties and Distribution of Ionic Conductances Generating Electroresponsiveness of Mammalian Inferior Olivary Neurons Invitro. J Physiol-London *315*, 569-584.
Long, M.A., Deans, M.R., Paul, D.L., and Connors, B.W. (2002). Rhythmicity without synchrony in the electrically uncoupled inferior olive. J Neurosci *22*, 10898-10905.
Meir, Y., Aharony, A., and Harris, A.B. (1989). Delocalization Transition in Two-Dimensional Quantum Percolation. Europhys Lett *10*, 275-278.
Roach, J.P., Pidde, A., Katz, E., Wu, J.X., Ognjanovski, N., Aton, S.J., and Zochowski, M.R. (2018). Resonance with subthreshold oscillatory drive organizes activity and optimizes learning in neural networks. P Natl Acad Sci USA *115*, E3017-E3025.
Shapir, Y., Aharony, A., and Harris, A.B. (1982). Localization and Quantum Percolation. Phys Rev Lett *49*, 486-489.
Tchumatchenko, T., and Clopath, C. (2014). Oscillations emerging from noise-driven steady state in networks with electrical synapses and subthreshold resonance. Nat Commun *5*.
Thomas, B.S.D., and Nakanishi, H. (2016). Two-dimensional quantum percolation with binary nonzero hopping integrals. Phys Rev E *94*.
Turecek, J., Han, V.Z., Carlson, V.C.C., Grant, K.A., and Welsh, J.P. (2016). Electrical Coupling and Synchronized Subthreshold Oscillations in the Inferior Olive of the Rhesus Macaque. J Neurosci *36*, 6497-6502.
V-Ghaffari, B., Kouhnavard, M., and Kitajima, T. (2016). Biophysical Properties of Subthreshold Resonance Oscillations and Subthreshold Membrane Oscillations in Neurons. J Biol Syst *24*, 561-575.

Figures

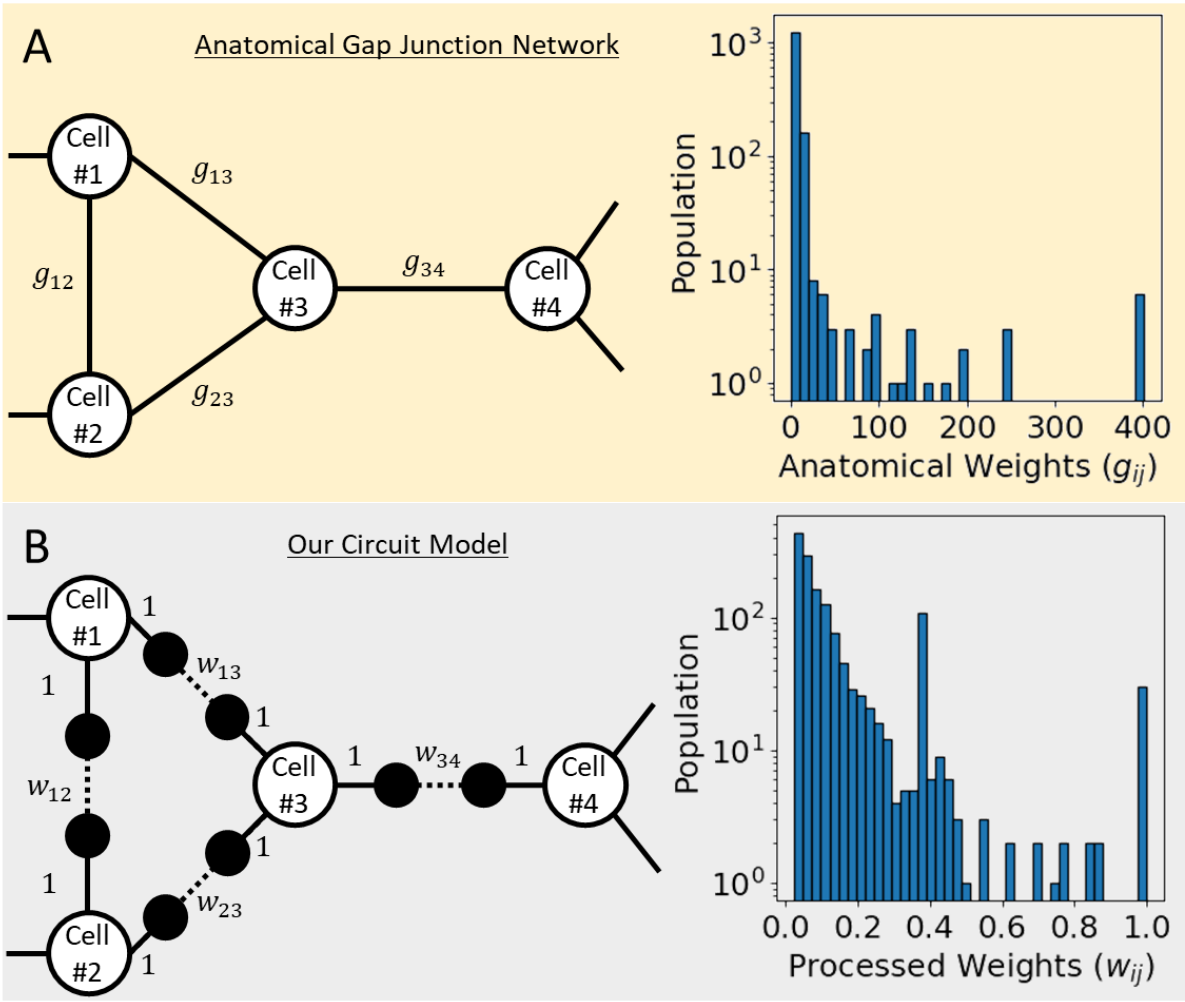

Figure 1. Anatomical gap junction network and our circuit model. (A) In the sample of the network diagram on the left, there are white-filled nodes stand for cells, and the edges of a solid line stand for the anatomical gap junction between them. The graph on the right is the distribution of 1,433 gap junction weights obtained from the connectome data of *C. elegans*. **(B)** In the sample of the network diagram on the left, equally spaced two virtual nodes were added between cells connected by a gap junction, and the virtual node is presented as a black-filled circle. The solid line stands for the connection between the cell and the virtual node that gave a weight of 1, and the dotted line stands for the connection between the two virtual nodes that gave our processed weight between 0 and 1. Our processed weights are calculated from the anatomical gap junction weights, and the graph on the right shows its distribution.

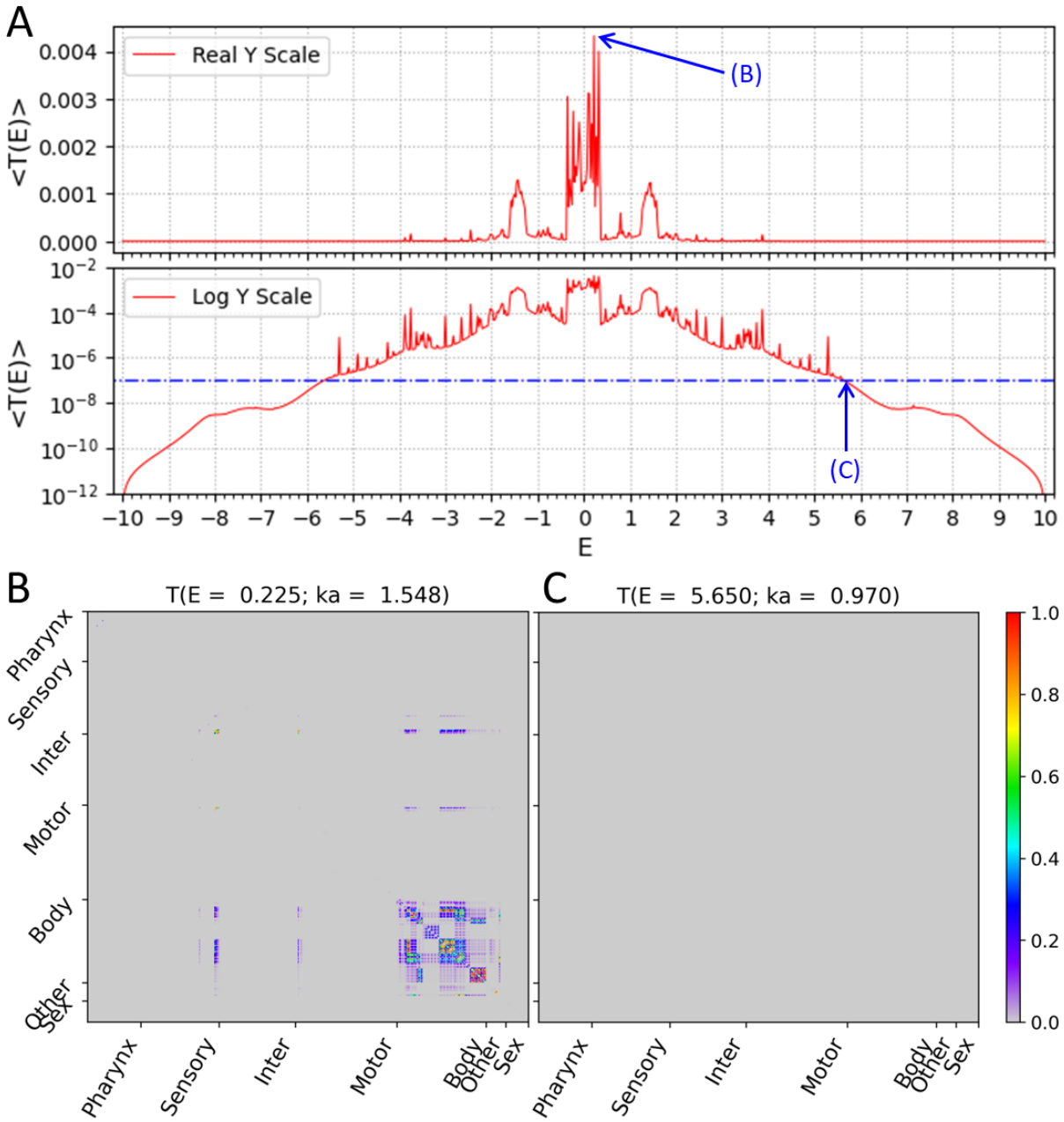

Figure 2. Wavenumber-dependent transmission coefficient. Average transmission coefficient for all cell-pairs as a function of *E* values (*E* value is a function of the wavenumber of the subthreshold wave). **(A)** The upper panel shows the average transmission coefficient graph on the Y-axis of the real scale and the lower panel shows the same graph on the Y-axis of the log scale. The reference value (10^{-7}) of the signal mobility edge is indicated in the lower panel as a dot-dash

line. **(B)** The transmission coefficient of all cell-pairs at $E = 0.225$ is represented as a heatmap, which is the highest average transmission coefficient in our result. **(C)** The transmission coefficient of all cell-pairs at $E = 5.650$ is represented as a heatmap, which is one of the signal mobility edges. **(B, C)** In heatmap, the X and Y axes are arranged according to the index of 469 cells, and the index follows that of the original connectome data. Instead of displaying all cell names, only seven cell types were indicated.

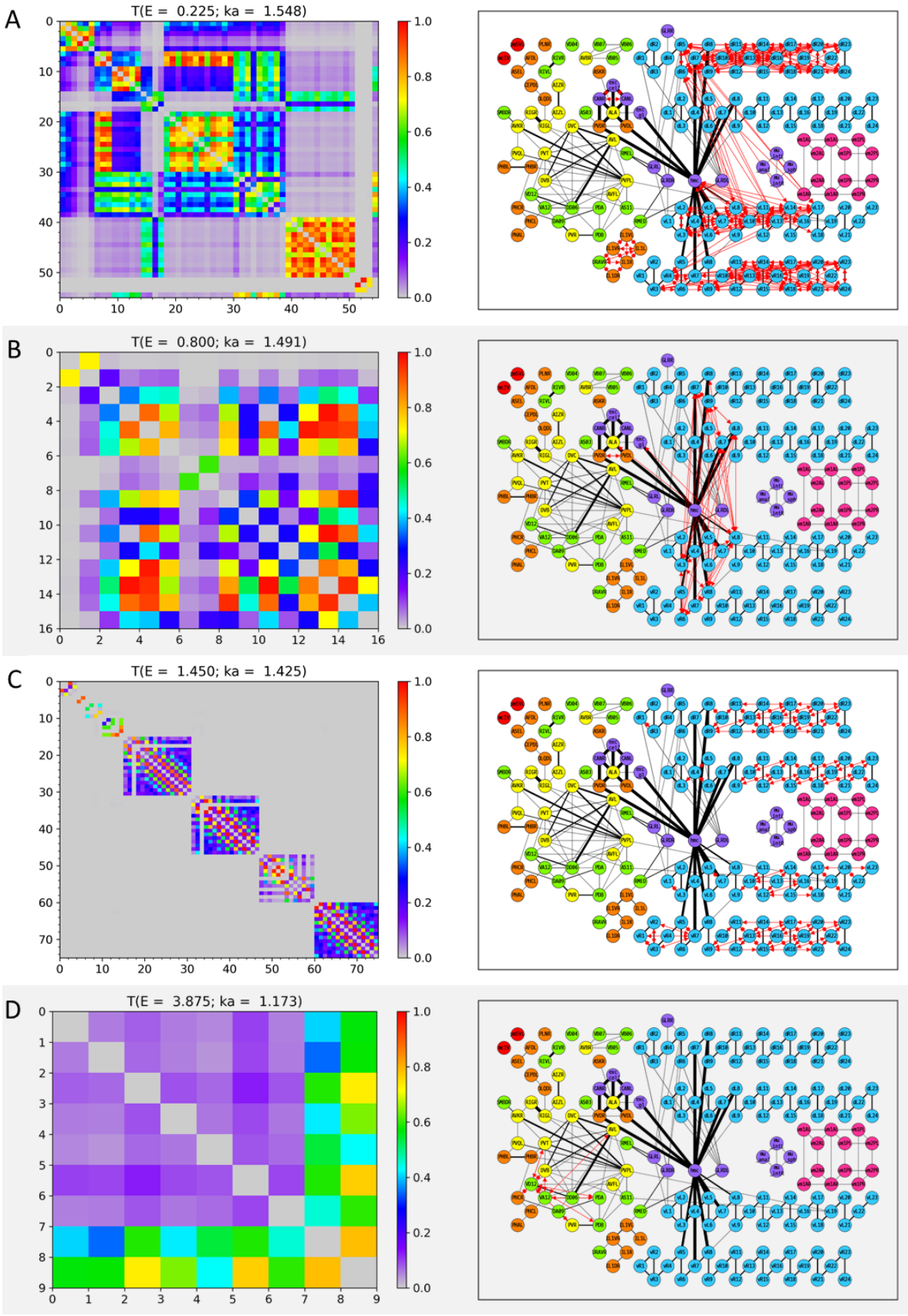
A
T(E = 0.225; ka = 1.548)
B
T(E = 0.800; ka = 1.491)
C
T(E = 1.450; ka = 1.425)
D
T(E = 3.875; ka = 1.173)

Figure 3. Wavenumber-dependent transmission map. The cell-pairs with strong transmission ($T_{ij}(E) > 0.5$) at **(A)** $E = 0.225$, **(B)** $E = 0.800$, **(C)** $E = 1.450$, and **(D)** $E = 3.875$ (or the corresponding wavenumbers) are shown, respectively. The left panels represent the transmission coefficient between cells belonging to the cell-pairs with strong transmission at each *E* value as a heatmap. Here, the X and Y axes are the cell index, and the cell name corresponding to the cell index can be found in Table S1-3. The right panels display the cell-pairs of strong transmission at each *E* value as red bidirectional arrows of the same thickness on the network diagram. In the network diagram, the cell name is written inside the circle that stands for each node (for the body-wall muscles, the cell name is abbreviated as follows; ex) dBWML1 → dL1), and the color of the node stands for the cell type (Red: Pharynx cells, Orange: Sensory neurons, Yellow: Inter neurons, Green: Motor neurons, Light blue: Body-wall muscles, Purple: Other end organs, Magenta: Sex-specific cells). Edges indicated by black solid lines stand for the electrical synapses among the cells, and the thickness of the edges is proportional to our processed weight. In the network diagram, only 173 cells that belonged to the cell-pair with strong transmission at least once in positive *E* values are represented, and the remaining cells and the electrical synapses by them are omitted from display. The virtual nodes of our circuit are also omitted from the display.

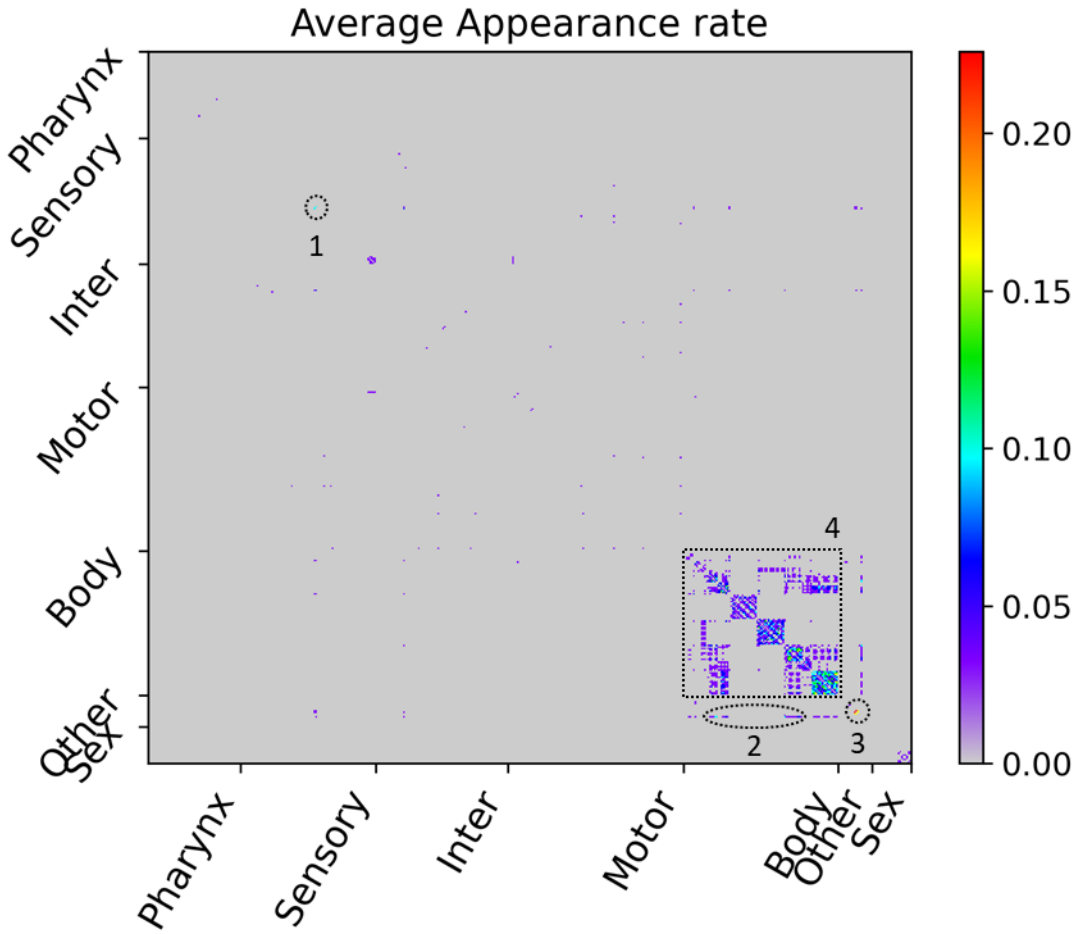

Figure 4. Average appearance rate as cell-pair with strong transmission in the WDTMs. The average appearance rate of all cell-pairs is represented as a heatmap. Here, the X and Y axes are arranged according to the index of 469 cells, and the index follows that of the original connectome data. Instead of displaying all cell names, only seven cell types were indicated. The highest rate is $7/31 \approx 0.23$, and four cell-pair groups showing rates of $3/31 \approx 0.1$ or higher are identified and numbered in the heatmap. (1) PVDL-PVDR pair, (2) hmc-vBWML6, hmc-vBWML7, and hmc-vBWML8 pairs, (3) CANL-CANR, CANL-exc_cell, and CANR-exc_cell pairs, (4) many cell-pairs of intra-strand of the body-wall muscles.

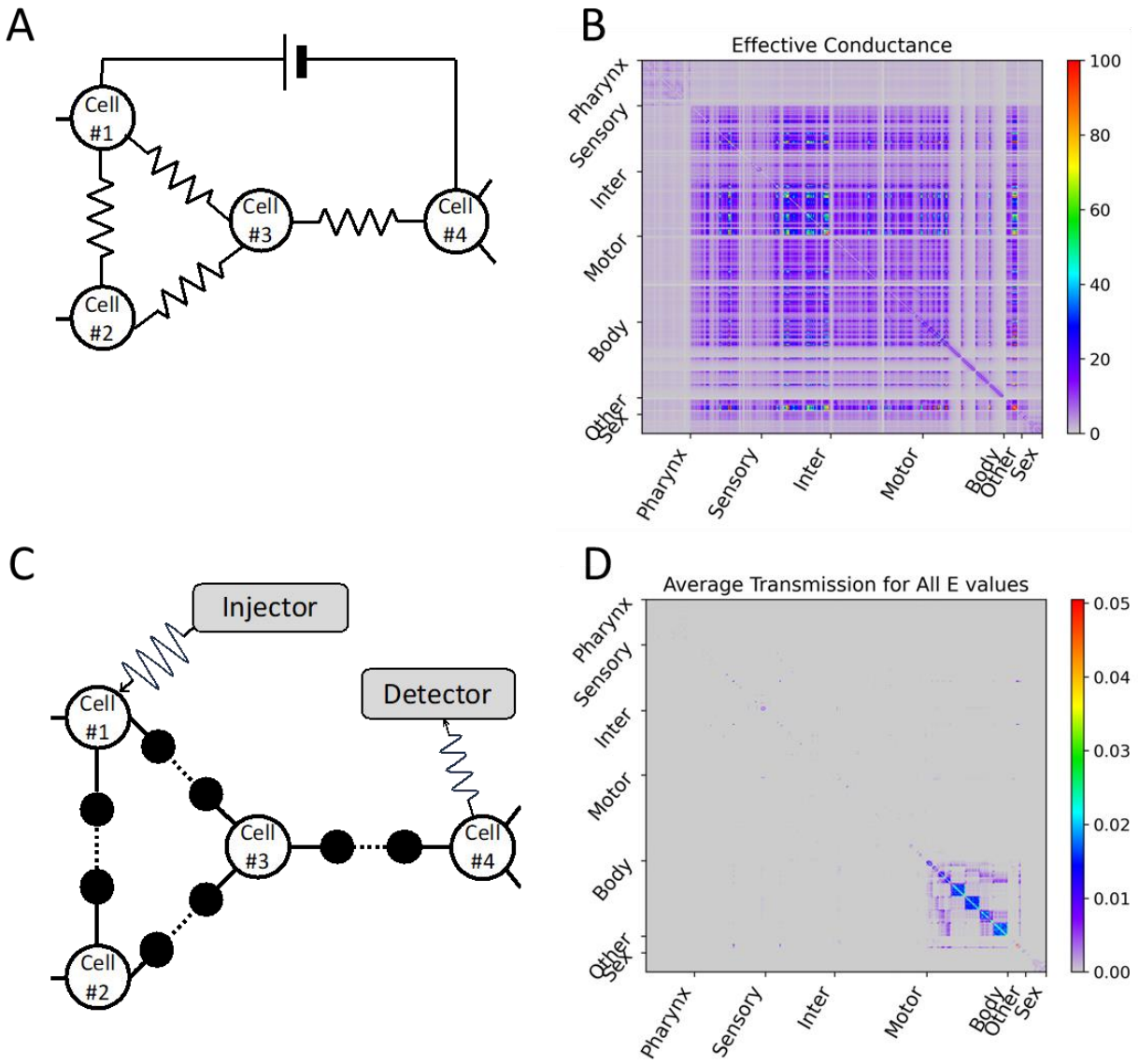

Figure 5. Differences depending on whether the electrical synapse network model considers interference. (A) In the electrical synapse network model without considering interference, when the electrical synapse is treated as an electrical resistor, the effective conductance (the reciprocal of the effective resistance) experienced by the external direct current power applied to an arbitrary cell-pair was calculated, and this value was represented as **(B)** a heatmap for all cell-pairs. **(C)** In our circuit considering interference of wave signals, the average transmission coefficient for all *E* values (or all wavenumbers) of an arbitrary cell-pair was calculated, and this value was represented as **(D)** a heatmap for all cell-pairs. **(B, D)** In heatmap, the X and Y axes are arranged according to

701 the index of 469 cells, and the index follows that of the original connectome data. Instead of
702 displaying all cell names, only seven cell types are indicated.

Supplementary Materials

Auxiliary paragraphs 1 to 3,

Figs. S1 to S10,

Tables S1 to S4.

Auxiliary paragraph 1.

The 31 specific *E* values in this study were not fixed and were of a property that can change as a researcher adjusts the resolution of the *E* value. Perhaps the higher the resolution of the *E* value, the more specific *E* values will be found. And it was arbitrary that our reference value for strong transmission was 0.5, and this reference value can be raised or lowered depending on the researcher's intention, and the lower the reference value, the greater the number of cell-pairs with strong transmission will be found.

Auxiliary paragraph 2.

Because of the omitted the rest of cells and their electrical synapses in the network diagram, some nodes in the diagram look like remote islands, but it should be remembered that the 173 cells were connected as one large cluster through both the drawn and the omitted electrical synapses.

Auxiliary paragraph 3.

Because the number of the cell-pairs of intra-body-wall muscles was overwhelmingly large and it was relatively easy to measure the distance compared to those of other cell-pairs, the investigation for the distance excluded them (for example, the distance of two body-wall muscles in the same strand easily calculate from the given number in the name of the muscles).

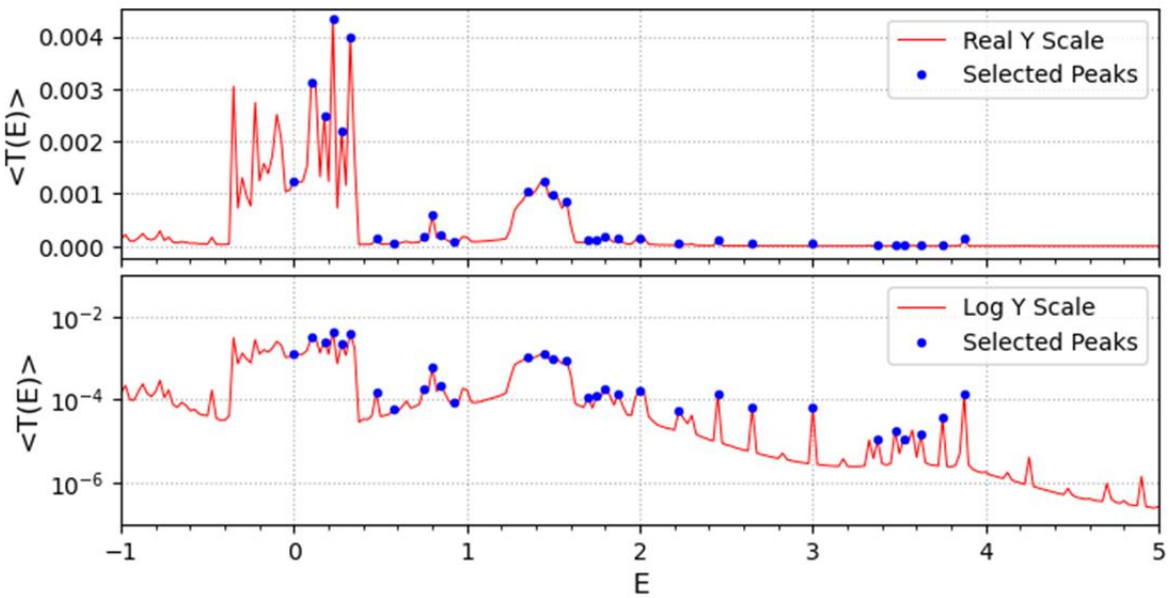

Figure S1. Selected $\langle T(E) \rangle$ peaks. The 31 selected peaks are shown as dots on the graph of the average transmission coefficient for all cell-pairs. To make the dots more visible, only the *E* value range of [-1, 5] was drawn out of the total [-10, 10]. The upper panel shows the dots and the graph on the Y-axis of the real scale and the lower panel shows the same things on the Y-axis of the log scale.

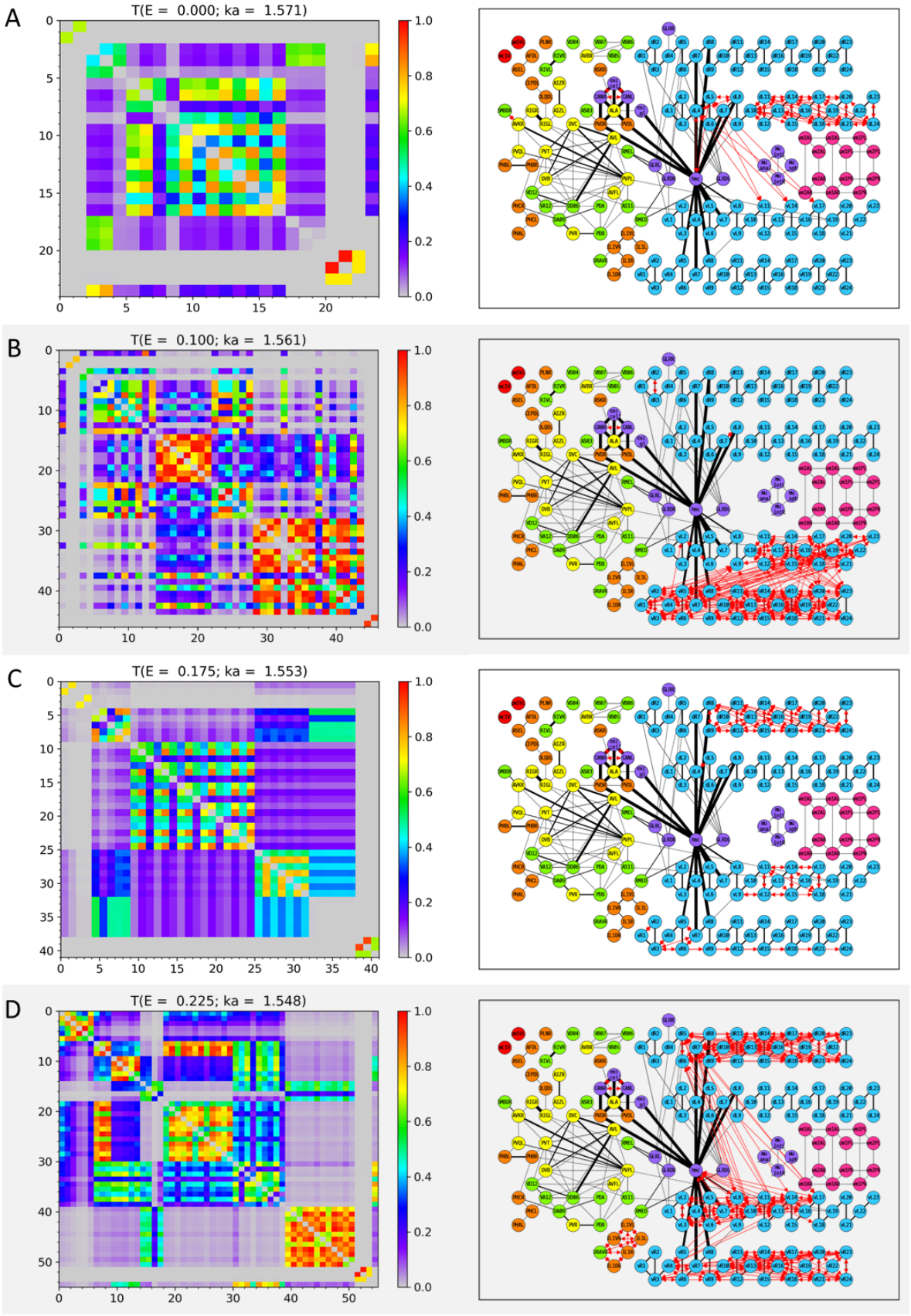
A
T(E = 0.000; ka = 1.571)
B
T(E = 0.100; ka = 1.561)
C
T(E = 0.175; ka = 1.553)
D
T(E = 0.225; ka = 1.548)

Figure S2. Wavenumber-dependent transmission map. The cell-pairs with strong transmission ($T_{ij}(E) > 0.5$) at **(A)** $E = 0.000$, **(B)** $E = 0.100$, **(C)** $E = 0.175$, and **(D)** $E = 0.225$ (or the corresponding wavenumbers) are shown, respectively. The left panels represent the transmission coefficient between cells belonging to the cell-pairs with strong transmission at each *E* value as a heatmap. Here, the X and Y axes are the cell index, and the cell name corresponding to the cell index can be found in Table S1-3. The right panels display the cell-pairs of strong transmission at each *E* value as red bidirectional arrows of the same thickness on the network diagram. In the network diagram, the cell name is written inside the circle that stands for each node (for the body-wall muscles, the cell name is abbreviated as follows; ex) dBWML1 → dL1), and the color of the node stands for the cell type (Red: Pharynx cells, Orange: Sensory neurons, Yellow: Inter neurons, Green: Motor neurons, Light blue: Body-wall muscles, Purple: Other end organs, Magenta: Sex-specific cells). Edges indicated by black solid lines stand for the electrical synapses among the cells, and the thickness of the edges is proportional to our processed weight. In the network diagram, only 173 cells that belonged to the cell-pair with strong transmission at least once in positive *E* values are represented, and the remaining cells and the electrical synapses by them are omitted from display. The virtual nodes of our circuit are also omitted from the display.

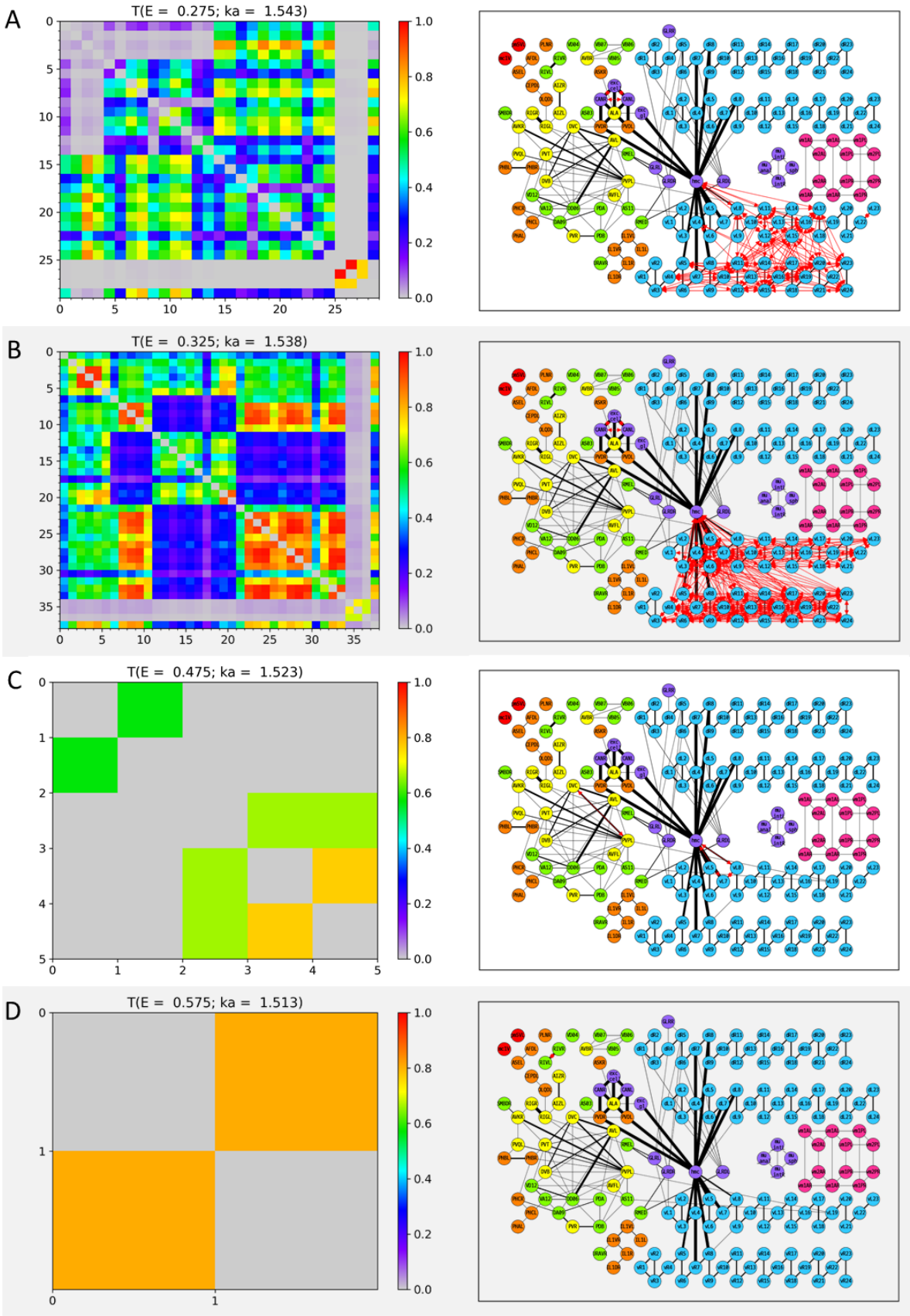
A
T(E = 0.275; ka = 1.543)
B
T(E = 0.325; ka = 1.538)
C
T(E = 0.475; ka = 1.523)
D
T(E = 0.575; ka = 1.513)

Figure S3. Wavenumber-dependent transmission map. The cell-pairs with strong transmission ($T_{ij}(E) > 0.5$) at **(A)** $E = 0.275$, **(B)** $E = 0.325$, **(C)** $E = 0.475$, and **(D)** $E = 0.575$ (or the corresponding wavenumbers) are shown, respectively. The heatmaps of the left panels and the network diagram of the right panels are represented in the same way as in Fig. S2.

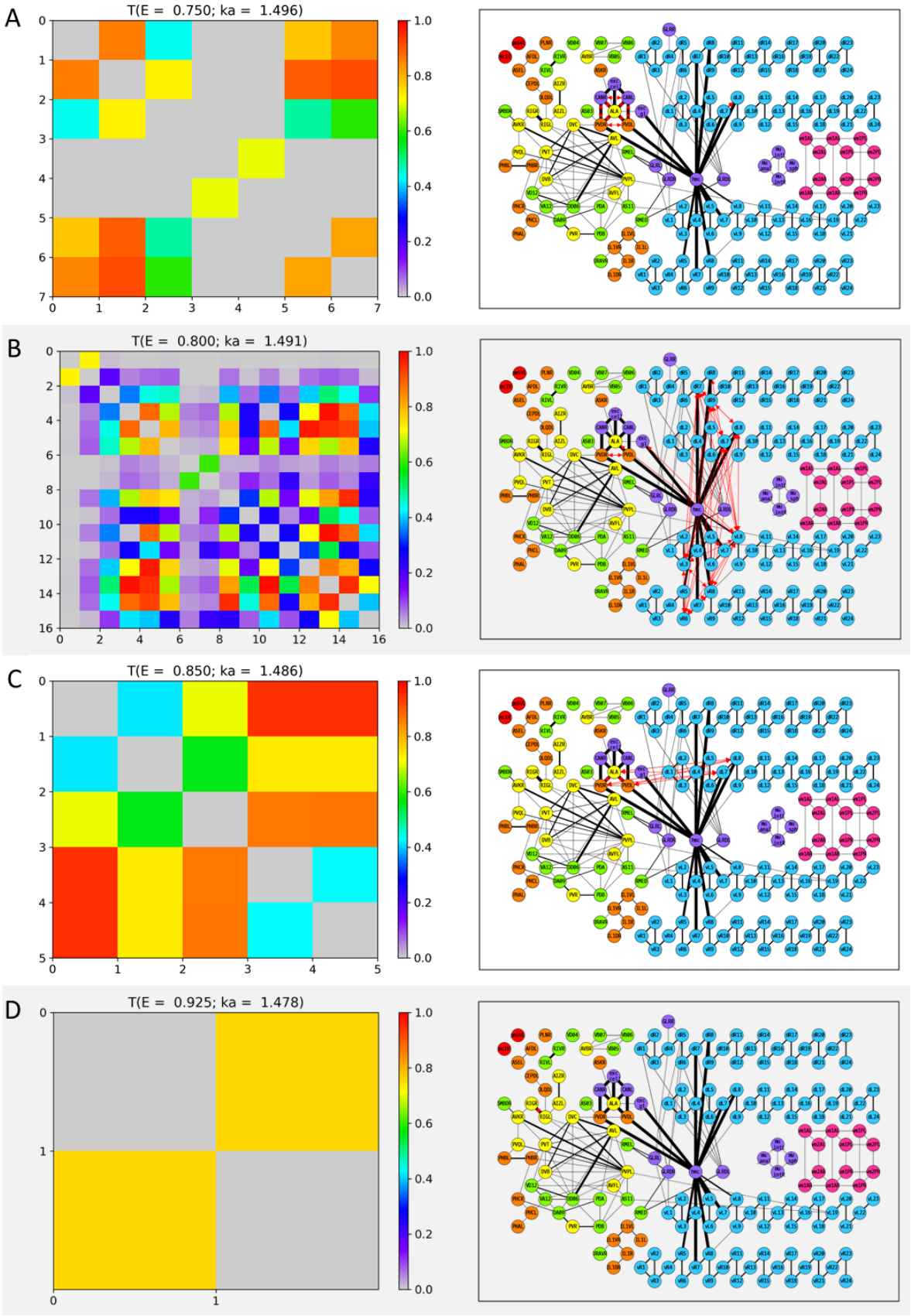
A
T(E = 0.750; ka = 1.496)
B
T(E = 0.800; ka = 1.491)
C
T(E = 0.850; ka = 1.486)
D
T(E = 0.925; ka = 1.478)

758

Figure S4. Wavenumber-dependent transmission map. The cell-pairs with strong transmission ($T_{ij}(E) > 0.5$) at **(A)** $E = 0.750$, **(B)** $E = 0.800$, **(C)** $E = 0.850$, and **(D)** $E = 0.925$ (or the corresponding wavenumbers) are shown, respectively. The heatmaps of the left panels and the network diagram of the right panels are represented in the same way as in Fig. S2.

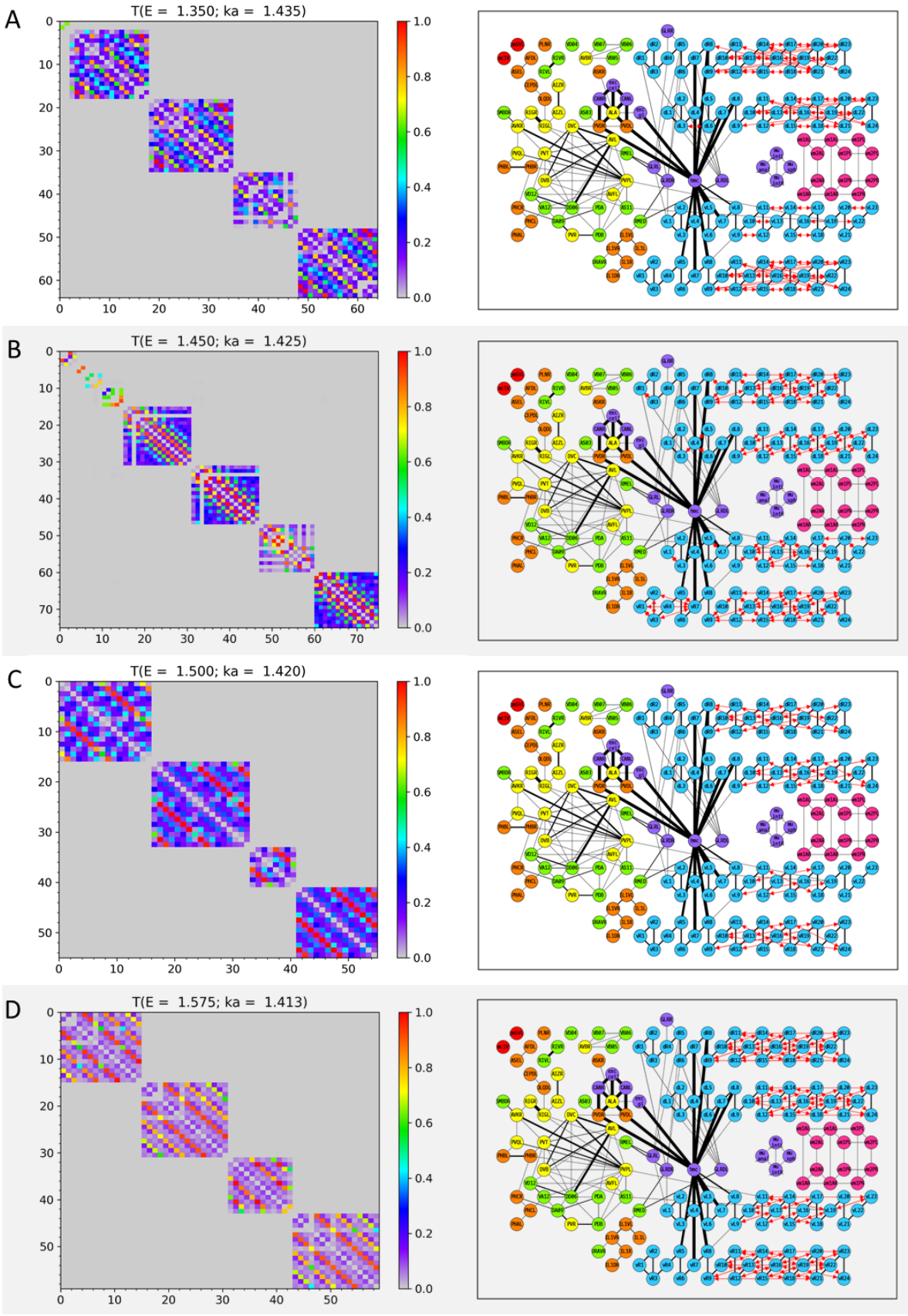
A
T(E = 1.350; ka = 1.435)
B
T(E = 1.450; ka = 1.425)
C
T(E = 1.500; ka = 1.420)
D
T(E = 1.575; ka = 1.413)

764

Figure S5. Wavenumber-dependent transmission map. The cell-pairs with strong transmission ($T_{ij}(E) > 0.5$) at **(A)** $E = 1.350$, **(B)** $E = 1.450$., **(C)** $E = 1.500$, and **(D)** $E = 1.575$ (or the corresponding wavenumbers) are shown, respectively. The heatmaps of the left panels and the network diagram of the right panels are represented in the same way as in Fig. S2.

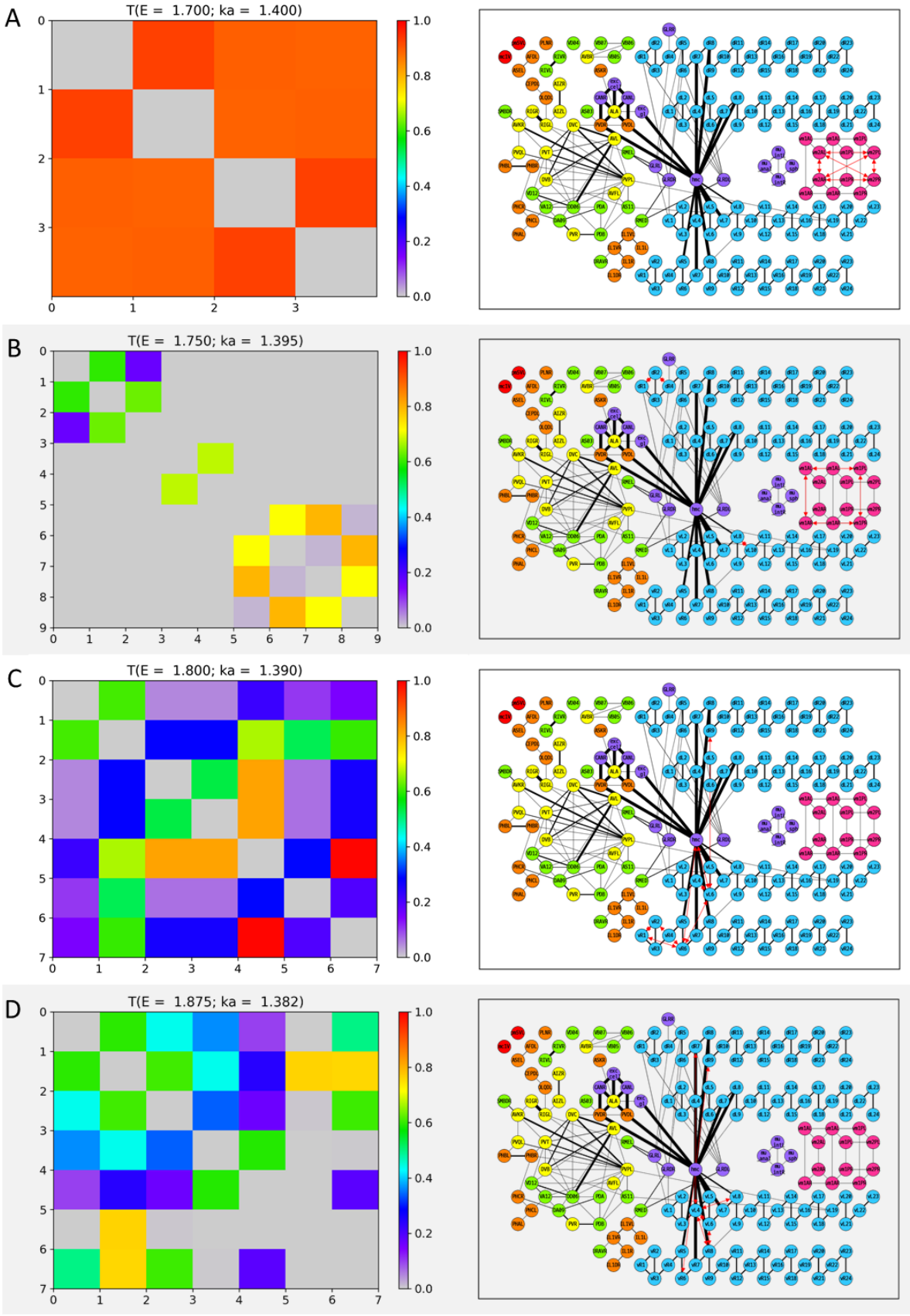
A
T(E = 1.700; ka = 1.400)
B
T(E = 1.750; ka = 1.395)
C
T(E = 1.800; ka = 1.390)
D
T(E = 1.875; ka = 1.382)

Figure S6. Wavenumber-dependent transmission map. The cell-pairs with strong transmission ($T_{ij}(E) > 0.5$) at **(A)** $E = 1.700$, **(B)** $E = 1.750$, **(C)** $E = 1.800$, and **(D)** $E = 1.875$ (or the corresponding wavenumbers) are shown, respectively. The heatmaps of the left panels and the network diagram of the right panels are represented in the same way as in Fig. S2.

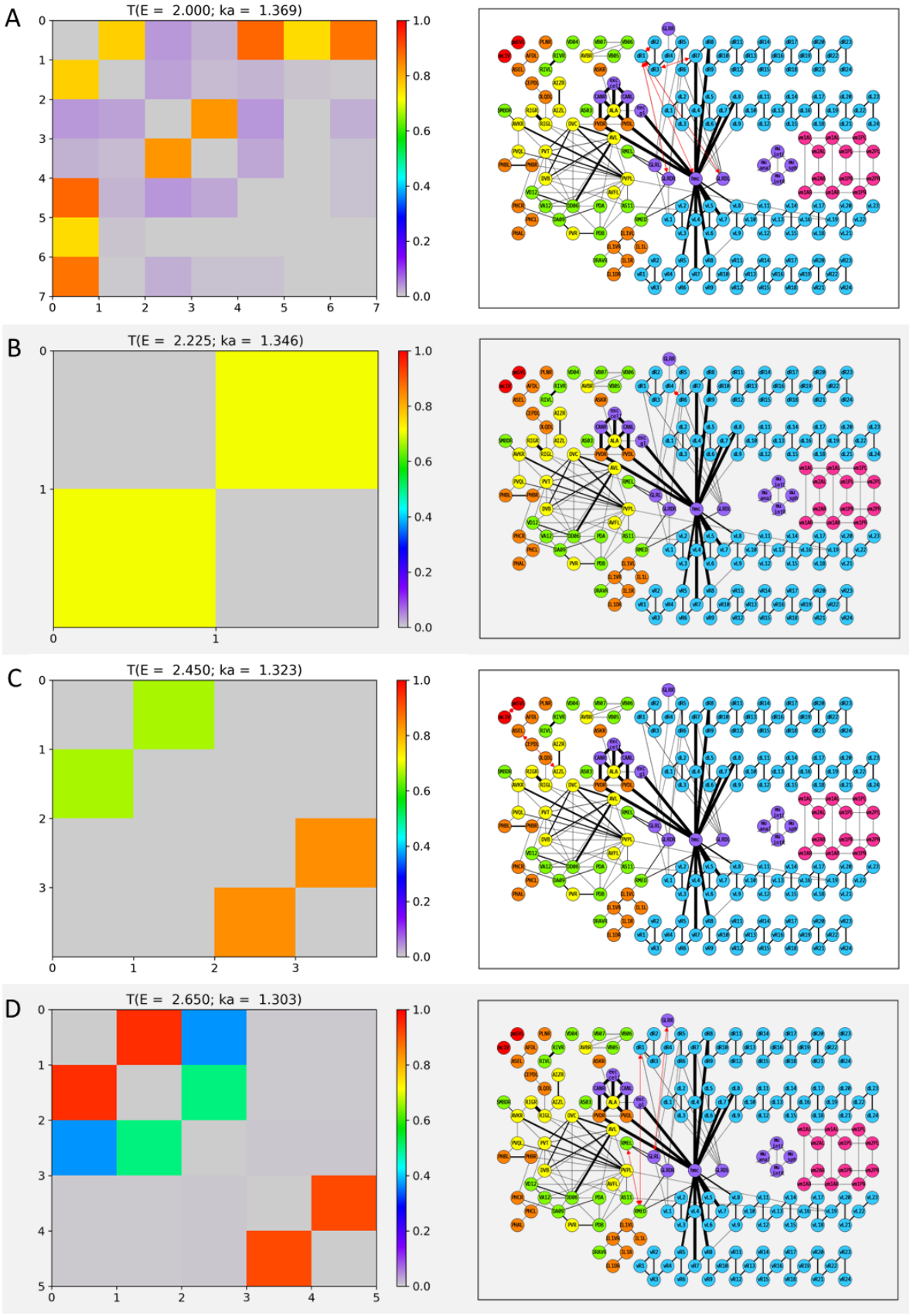
A
T(E = 2.000; ka = 1.369)
B
T(E = 2.225; ka = 1.346)
C
T(E = 2.450; ka = 1.323)
D
T(E = 2.650; ka = 1.303)

Figure S7. Wavenumber-dependent transmission map. The cell-pairs with strong transmission ($T_{ij}(E) > 0.5$) at **(A)** $E = 2.000$, **(B)** $E = 2.225$, **(C)** $E = 2.450$, and **(D)** $E = 2.650$ (or the corresponding wavenumbers) are shown, respectively. The heatmaps of the left panels and the network diagram of the right panels are represented in the same way as in Fig. S2.

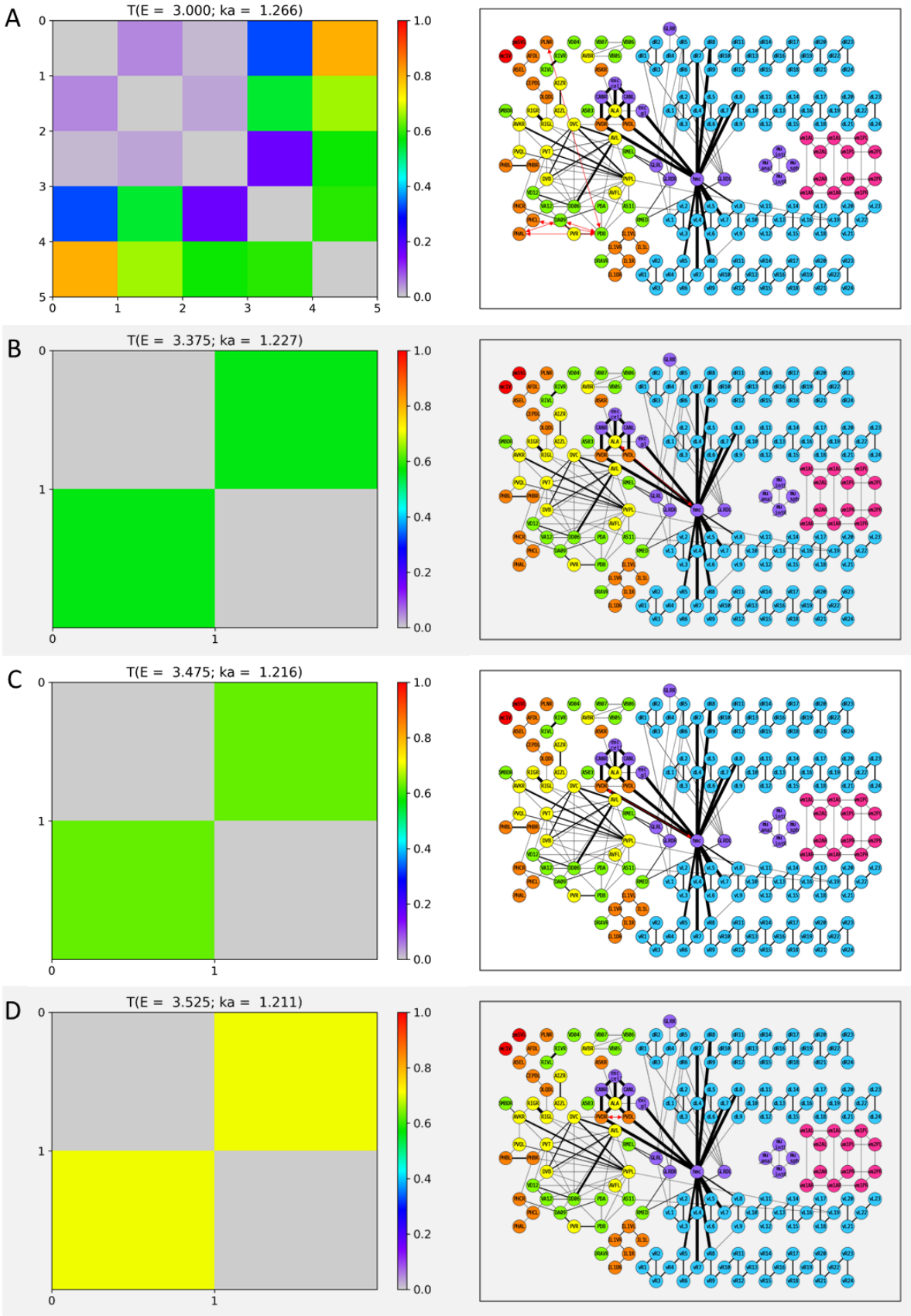
A
T(E = 3.000; ka = 1.266)
B
T(E = 3.375; ka = 1.227)
C
T(E = 3.475; ka = 1.216)
D
T(E = 3.525; ka = 1.211)

782

Figure S8. Wavenumber-dependent transmission map. The cell-pairs with strong transmission ($T_{ij}(E) > 0.5$) at **(A)** $E = 3.000$, **(B)** $E = 3.375$, **(C)** $E = 3.475$, and **(D)** $E = 3.525$ (or the corresponding wavenumbers) are shown, respectively. The heatmaps of the left panels and the network diagram of the right panels are represented in the same way as in Fig. S2.

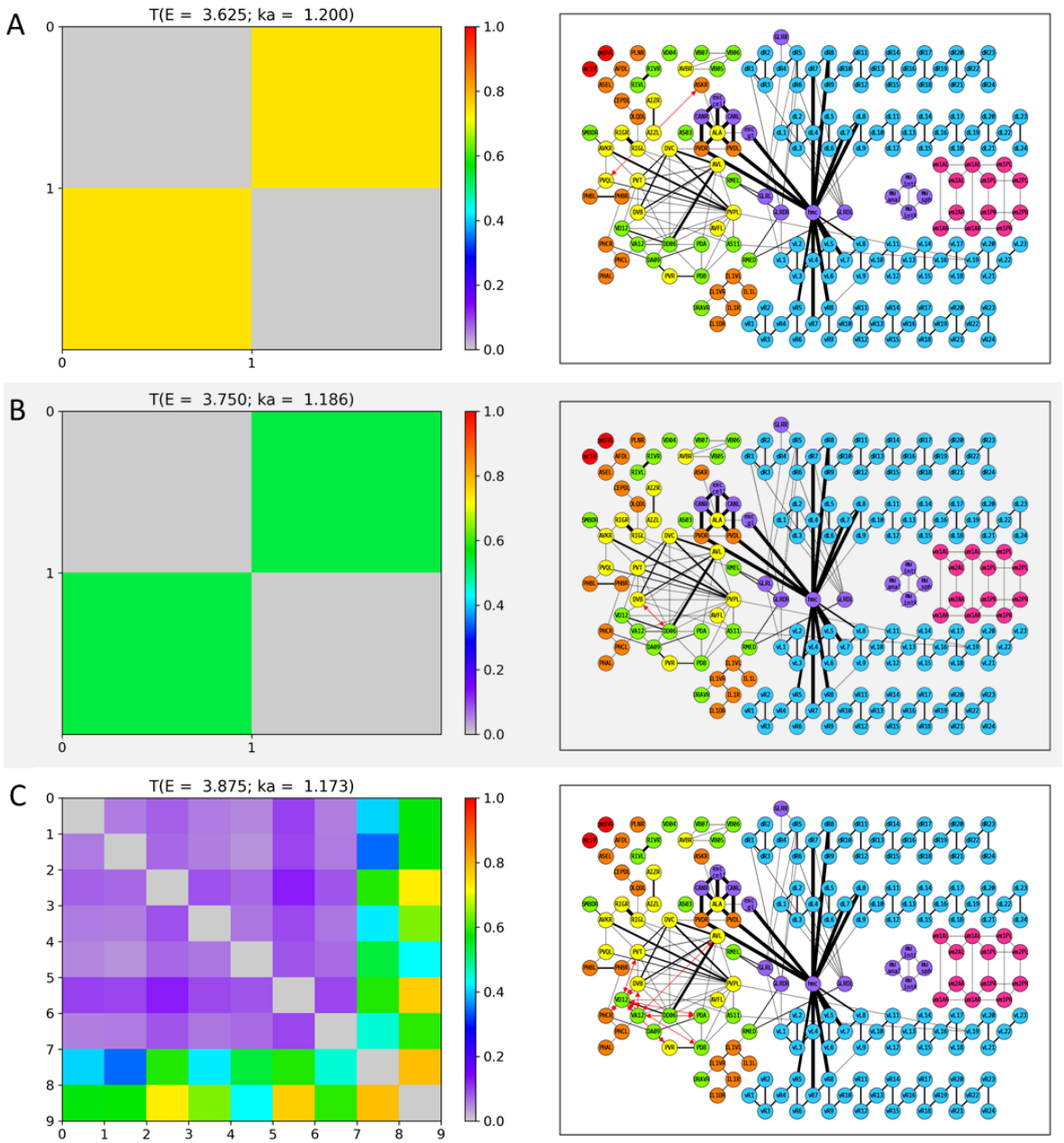

Figure S9. Wavenumber-dependent transmission map. The cell-pairs with strong transmission ($T_{ij}(E) > 0.5$) at **(A)** $E = 3.625$, **(B)** $E = 3.750$, and **(C)** $E = 3.875$ (or the corresponding wavenumbers) are shown, respectively. The heatmaps of the left panels and the network diagram of the right panels are represented in the same way as in Fig. S2.

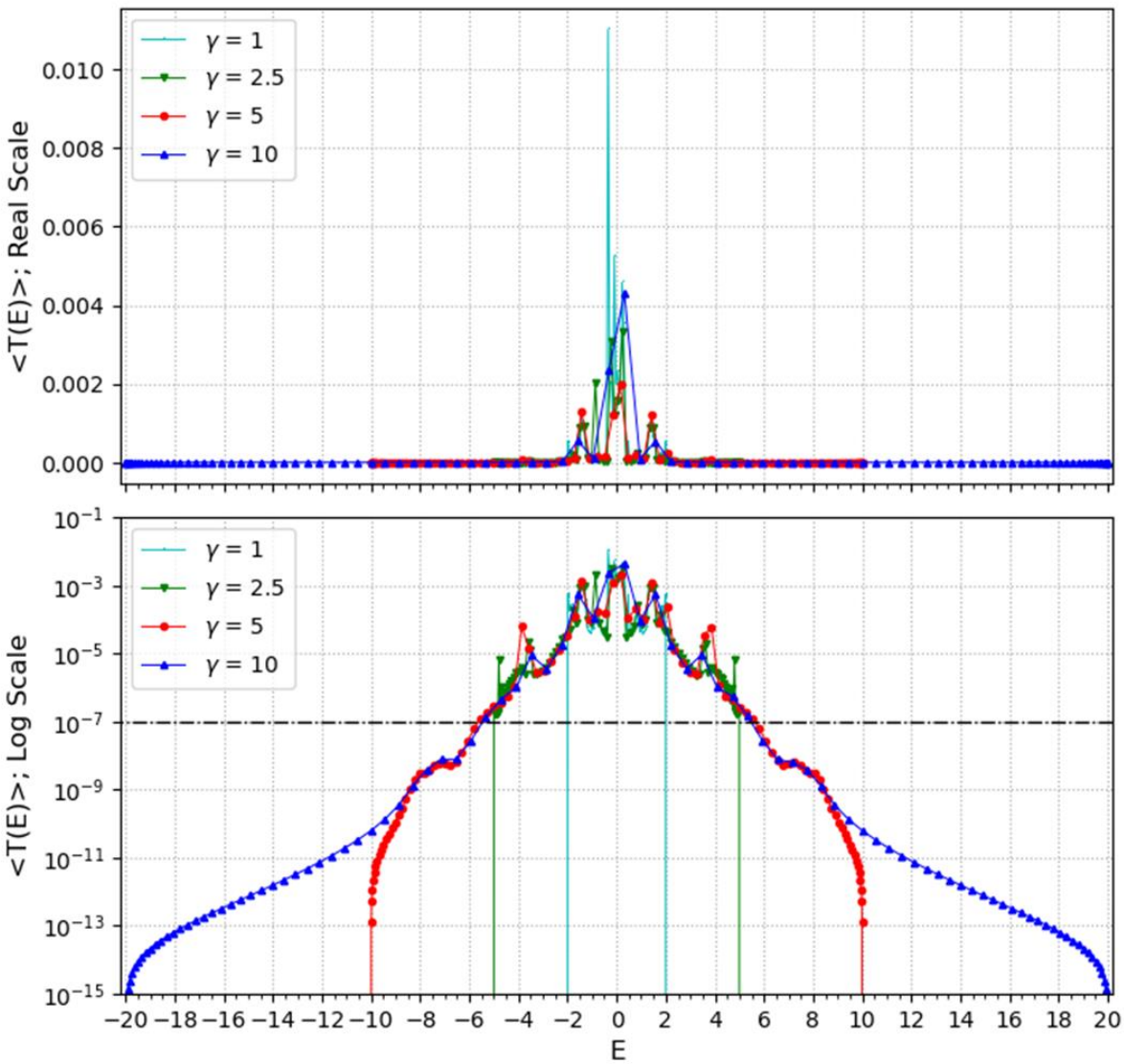

Figure S10. Searching for optimal gamma. The average transmission coefficient for all cell-pairs as a function of *E* value (*E* value is a function of both γ and wavenumber *k*) was calculated under the four γ conditions (1, 2.5, 5, 10), respectively. Here, the wavenumbers used the same set as a hundred values equally spaced in the range of $[0,\ \pi/a]$. The upper panel shows the average transmission coefficient graphs as the Y-axis of the real scale and the lower panel shows the same graphs as the Y-axis of the log scale. The reference value (10^{-7}) of the signal mobility edge is shown in the lower panel as a dot-dash line.

E=0.000	ka=1.571
Index	Cell name
0	AVKR
1	SMBDR
2	dBWML4
3	dBWML5
4	dBWML8
5	dBWML10
6	dBWML11
7	dBWML12
8	dBWML13
9	dBWML14
10	dBWML15
11	dBWML17
12	dBWML18
13	dBWML20
14	dBWML21
15	dBWML23
16	dBWML24
17	vBWML11
18	vBWML14
19	vBWML17
20	CANL
21	CANR
22	exc_cell
23	hmc

E=0.100	ka=1.561
Index	Cell name
0	dBWML7
1	dBWMR2
2	dBWMR3
3	vBWML2
4	vBWML6
5	vBWMR1
6	vBWMR2
7	vBWMR3
8	vBWMR4
9	vBWMR5
10	vBWMR6
11	vBWMR7
12	dBWML8
13	vBWML9
14	vBWML10
15	vBWML11
16	vBWML12
17	vBWML13
18	vBWML15
19	vBWML16
20	vBWML17
21	vBWML18
22	vBWML19
23	vBWML20
24	vBWML21
25	vBWML22
26	vBWML23
27	vBWMR8
28	vBWMR9
29	vBWMR10
30	vBWMR11
31	vBWMR12
32	vBWMR13
33	vBWMR14
34	vBWMR15
35	vBWMR16
36	vBWMR17
37	vBWMR18
38	vBWMR19
39	vBWMR20
40	vBWMR21
41	vBWMR22
42	vBWMR23
43	vBWMR24
44	CANL
45	CANR

E=0.175	ka=1.553
Index	Cell name
0	dBWML4
1	dBWML5
2	vBWMR1
3	vBWMR2
4	vBWMR3
5	vBWMR4
6	vBWMR5
7	vBWMR6
8	vBWMR7
9	dBWMR8
10	dBWMR9
11	dBWMR10
12	dBWMR11
13	dBWMR12
14	dBWMR13
15	dBWMR14
16	dBWMR15
17	dBWMR16
18	dBWMR17
19	dBWMR18
20	dBWMR19
21	dBWMR20
22	dBWMR21
23	dBWMR23
24	dBWMR24
25	vBWML9
26	vBWML11
27	vBWML12
28	vBWML14
29	vBWML15
30	vBWML17
31	vBWML18
32	vBWMR9
33	vBWMR12
34	vBWMR15
35	vBWMR18
36	vBWMR21
37	vBWMR24
38	CANL
39	CANR
40	exc_cell

E=0.225	ka=1.548
Index	Cell name
0	IL1DR
1	IL1L
2	IL1R
3	IL1VL
4	IL1VR
5	URAVR
6	dBWMR5
7	dBWMR6
8	dBWMR7
9	vBWML2
10	vBWML3
11	vBWML4
12	vBWML6
13	vBWML7
14	vBWMR3
15	vBWMR4
16	vBWMR6
17	vBWMR7
18	dBWMR9
19	dBWMR10
20	dBWMR11
21	dBWMR13
22	dBWMR14
23	dBWMR16
24	dBWMR17
25	dBWMR18
26	dBWMR20
27	dBWMR21
28	dBWMR23
29	dBWMR24
30	vBWML8
31	vBWML9
32	vBWML10
33	vBWML11
34	vBWML13
35	vBWML14
36	vBWML16
37	vBWML17
38	vBWML18
39	vBWMR9
40	vBWMR10
41	vBWMR11
42	vBWMR13
43	vBWMR14
44	vBWMR16
45	vBWMR17
46	vBWMR18
47	vBWMR20
48	vBWMR21
49	vBWMR23
50	vBWMR24
51	CANL
52	CANR
53	exc_cell
54	hmc

E=0.275	ka=1.543
Index	Cell name
0	vBWML4
1	vBWMR3
2	vBWMR4
3	vBWMR5
4	vBWML8
5	vBWML10
6	vBWML11
7	vBWML12
8	vBWML13
9	vBWML15
10	vBWML16
11	vBWML17
12	vBWML22
13	vBWML23
14	vBWMR10
15	vBWMR11
16	vBWMR12
17	vBWMR14
18	vBWMR15
19	vBWMR16
20	vBWMR19
21	vBWMR20
22	vBWMR21
23	vBWMR23
24	vBWMR24
25	CANL
26	CANR
27	exc_cell
28	hmc

E=0.325	ka=1.538
Index	Cell name
0	vBWML1
1	vBWML3
2	vBWML4
3	vBWML5
4	vBWML6
5	vBWML7
6	vBWMR3
7	vBWMR4
8	vBWMR5
9	vBWMR6
10	vBWMR7
11	vBWML10
12	vBWML11
13	vBWML12
14	vBWML16
15	vBWML17
16	vBWML18
17	vBWML19
18	vBWML21
19	vBWML22
20	vBWML23
21	vBWMR9
22	vBWMR10
23	vBWMR11
24	vBWMR12
25	vBWMR13
26	vBWMR16
27	vBWMR17
28	vBWMR18
29	vBWMR19
30	vBWMR20
31	vBWMR22
32	vBWMR23
33	vBWMR24
34	CANL
35	CANR
36	exc_cell
37	hmc

E=0.475	ka=1.523
Index	Cell name
0	PVPL
1	DVC
2	vBWML7
3	vBWML8
4	hmc

E=0.575	ka=1.513
Index	Cell name
0	RIVL
1	RIVR

Table S1. Cell names corresponding to the indices in the heatmaps for wavenumber-dependent transmission map. Each two columns shows the index and the corresponding cell name of the cells that belonged to the cell-pairs with strong transmission at the *E* value (or the corresponding wavenumber) indicated in the first row. The color painted on the name box stands for the cell type (Red: Pharynx cells, Orange: Sensory neurons, Yellow: Inter neurons, Green: Motor neurons, Light blue: Body-wall muscles, Purple: Other end organs, Magenta: Sex-specific cells).

E=0.750	ka=1.496
Index	Cell name
0	PVDL
1	PVDR
2	ALA
3	dBWML7
4	dBWML8
5	CANL
6	CANR

E=0.800	ka=1.491
Index	Cell name
0	PVDL
1	PVDR
2	ALA
3	dBWML7
4	dBWMR7
5	vBWML3
6	vBWML5
7	vBWML7
8	vBWMR6
9	vBWMR7
10	dBWML8
11	dBWMR8
12	dBWMR9
13	vBWML8
14	vBWMR8
15	exc_gl

E=0.850	ka=1.486
Index	Cell name
0	PVDL
1	PVDR
2	ALA
3	dBWML7
4	dBWML8

E=0.925	ka=1.478
Index	Cell name
0	RIGL
1	RIGR

E=1.350	ka=1.435
Index	Cell name
0	dBWML3
1	dBWML6
2	dBWML9
3	dBWML10
4	dBWML11
5	dBWML12
6	dBWML13
7	dBWML14
8	dBWML15
9	dBWML16
10	dBWML17
11	dBWML18
12	dBWML19
13	dBWML20
14	dBWML21
15	dBWML22
16	dBWML23
17	dBWML24
18	dBWMR8
19	dBWMR9
20	dBWMR10
21	dBWMR11
22	dBWMR12
23	dBWMR13
24	dBWMR14
25	dBWMR15
26	dBWMR16
27	dBWMR17
28	dBWMR18
29	dBWMR19
30	dBWMR20
31	dBWMR21
32	dBWMR22
33	dBWMR23
34	dBWMR24
35	vBWML9
36	vBWML10
37	vBWML11
38	vBWML12
39	vBWML13
40	vBWML14
41	vBWML15
42	vBWML16
43	vBWML17
44	vBWML18
45	vBWML20
46	vBWML22
47	vBWML23
48	vBWMR9
49	vBWMR10
50	vBWMR11
51	vBWMR12
52	vBWMR13
53	vBWMR14
54	vBWMR15
55	vBWMR16
56	vBWMR17
57	vBWMR18
58	vBWMR19
59	vBWMR20
60	vBWMR21
61	vBWMR22
62	vBWMR23
63	vBWMR24

E=1.450	ka=1.425
Index	Cell name
0	dBWML3
1	dBWML4
2	dBWML5
3	dBWML6
4	dBWMR1
5	dBWMR3
6	vBWML1
7	vBWML3
8	vBWML5
9	vBWML7
10	vBWMR1
11	vBWMR2
12	vBWMR3
13	vBWMR5
14	vBWMR7
15	dBWML9
16	dBWML10
17	dBWML11
18	dBWML12
19	dBWML13
20	dBWML14
21	dBWML15
22	dBWML16
23	dBWML17
24	dBWML18
25	dBWML19
26	dBWML20
27	dBWML21
28	dBWML22
29	dBWML23
30	dBWML24
31	dBWMR8
32	dBWMR9
33	dBWMR10
34	dBWMR11
35	dBWMR13
36	dBWMR14
37	dBWMR15
38	dBWMR16
39	dBWMR17
40	dBWMR18
41	dBWMR19
42	dBWMR20
43	dBWMR21
44	dBWMR22
45	dBWMR23
46	dBWMR24
47	vBWML9
48	vBWML10
49	vBWML11
50	vBWML12
51	vBWML14
52	vBWML16
53	vBWML17
54	vBWML18
55	vBWML19
56	vBWML20
57	vBWML21
58	vBWML22
59	vBWML23
60	vBWMR9
61	vBWMR11
62	vBWMR12
63	vBWMR13
64	vBWMR14
65	vBWMR15
66	vBWMR16
67	vBWMR17
68	vBWMR18
69	vBWMR19
70	vBWMR20
71	vBWMR21
72	vBWMR22
73	vBWMR23
74	vBWMR24

E=1.500	ka=1.420
Index	Cell name
0	dBWML9
1	dBWML10
2	dBWML11
3	dBWML12
4	dBWML13
5	dBWML14
6	dBWML15
7	dBWML16
8	dBWML17
9	dBWML18
10	dBWML19
11	dBWML20
12	dBWML21
13	dBWML22
14	dBWML23
15	dBWML24
16	dBWMR8
17	dBWMR9
18	dBWMR10
19	dBWMR11
20	dBWMR12
21	dBWMR13
22	dBWMR14
23	dBWMR15
24	dBWMR16
25	dBWMR17
26	dBWMR18
27	dBWMR19
28	dBWMR20
29	dBWMR21
30	dBWMR22
31	dBWMR23
32	dBWMR24
33	vBWML9
34	vBWML10
35	vBWML11
36	vBWML12
37	vBWML16
38	vBWML17
39	vBWML18
40	vBWML19
41	vBWMR9
42	vBWMR10
43	vBWMR11
44	vBWMR12
45	vBWMR13
46	vBWMR14
47	vBWMR16
48	vBWMR17
49	vBWMR18
50	vBWMR19
51	vBWMR20
52	vBWMR21
53	vBWMR23
54	vBWMR24

E=1.575	ka=1.413
Index	Cell name
0	dBWML10
1	dBWML11
2	dBWML12
3	dBWML13
4	dBWML14
5	dBWML15
6	dBWML16
7	dBWML17
8	dBWML18
9	dBWML19
10	dBWML20
11	dBWML21
12	dBWML22
13	dBWML23
14	dBWML24
15	dBWMR9
16	dBWMR10
17	dBWMR11
18	dBWMR12
19	dBWMR13
20	dBWMR14
21	dBWMR15
22	dBWMR16
23	dBWMR17
24	dBWMR18
25	dBWMR19
26	dBWMR20
27	dBWMR21
28	dBWMR22
29	dBWMR23
30	dBWMR24
31	vBWML9
32	vBWML10
33	vBWML11
34	vBWML12
35	vBWML13
36	vBWML14
37	vBWML15
38	vBWML16
39	vBWML17
40	vBWML18
41	vBWML19
42	vBWML23
43	vBWMR9
44	vBWMR10
45	vBWMR11
46	vBWMR12
47	vBWMR13
48	vBWMR14
49	vBWMR15
50	vBWMR16
51	vBWMR17
52	vBWMR18
53	vBWMR19
54	vBWMR20
55	vBWMR21
56	vBWMR22
57	vBWMR23
58	vBWMR24

Table S2. Cell names corresponding to the indices in the heatmaps for wavenumber-dependent transmission map. It is represented in the same way as Table S1.

E=1.700	ka=1.400
Index	Cell name
0	vm2AL
1	vm2AR
2	vm2PL
3	vm2PR

E=1.750	ka=1.395
Index	Cell name
0	dBWMR1
1	dBWMR2
2	dBWMR4
3	vBWML8
4	vBWML10
5	vm1AL
6	vm1AR
7	vm1PL
8	vm1PR

E=1.800	ka=1.390
Index	Cell name
0	vBWML4
1	vBWML6
2	vBWMR1
3	vBWMR2
4	vBWMR6
5	dBWMR9
6	hmc

E=1.875	ka=1.382
Index	Cell name
0	dBWMR7
1	vBWML4
2	vBWML6
3	vBWMR6
4	dBWMR9
5	vBWML8
6	vBWMR8

E=2.000	ka=1.369
Index	Cell name
0	dBWMR1
1	dBWMR2
2	dBWMR3
3	dBWMR7
4	GLRDL
5	GLRDR
6	hmc

E=2.225	ka=1.346
Index	Cell name
0	dBWMR4
1	dBWMR6

E=2.450	ka=1.323
Index	Cell name
0	pm5VL
1	mc1V
2	ASEL
3	AIZL

E=2.650	ka=1.303
Index	Cell name
0	RMEL
1	RMED
2	dBWMR1
3	GLRL
4	GLRR

E=3.000	ka=1.266
Index	Cell name
0	PLNR
1	PHAL
2	PHCL
3	DA09
4	PDB

E=3.375	ka=1.227
Index	Cell name
0	ALA
1	hmc

E=3.475	ka=1.216
Index	Cell name
0	PVDR
1	hmc

E=3.525	ka=1.211
Index	Cell name
0	PVDL
1	PVDR

E=3.625	ka=1.200
Index	Cell name
0	ASKR
1	PVQL

E=3.750	ka=1.186
Index	Cell name
0	DVB
1	DD06

E=3.875	ka=1.173
Index	Cell name
0	PHCR
1	PVR
2	DVB
3	PVT
4	AVL
5	PDA
6	PDB
7	VA12
8	VD12

Table S3. Cell names corresponding to the indices in the heatmaps for wavenumber-dependent transmission map. It is represented in the same way as Table S1.

Distance	Cell names in the pair		Max(T(E))	E(ka)	ka
17	dBWMR24	hmc	0.912	0.125	1.558
17	vBWMR24	hmc	0.765	0.325	1.538
16	vBWMR23	hmc	0.797	0.325	1.538
15	dBWMR22	hmc	0.805	0.125	1.558
15	vBWMR22	hmc	0.603	0.325	1.538
14	dBWMR21	hmc	0.946	0.125	1.558
12	dBWMR19	hmc	0.892	0.125	1.558
12	vBWMR19	hmc	0.692	0.325	1.538
11	dBWMR18	hmc	0.731	0.125	1.558
11	vBWMR18	hmc	0.754	0.325	1.538
10	dBWMR17	hmc	0.645	0.125	1.558
10	vBWMR17	hmc	0.789	0.325	1.538
9	dBWMR16	hmc	0.936	0.125	1.558
9	vBWMR16	hmc	0.739	0.325	1.538
8	vBWML15	hmc	0.593	0.275	1.543
7	AVBR	dBWML12	0.601	1.000	1.471
7	dBWMR14	hmc	0.867	0.125	1.558
7	vBWML14	hmc	0.726	0.225	1.548
7	vBWML16	hmc	0.776	0.275	1.543
6	dBWMR13	hmc	0.900	0.125	1.558
6	vBWML13	hmc	0.832	0.225	1.548
6	vBWML17	hmc	0.801	0.225	1.548
6	vBWMR13	hmc	0.593	0.325	1.538
5	CEPDL	IL1R	0.716	0.050	1.566
5	AS11	vBWMR4	0.574	1.000	1.471
5	VD04	vBWML5	0.617	0.075	1.563
5	vBWML12	hmc	0.785	0.275	1.543
5	vBWML18	hmc	0.503	0.225	1.548
5	vBWMR12	hmc	0.743	0.325	1.538
4	CEPDL	IL1DR	0.757	0.050	1.566
4	OLQDL	IL1R	0.716	0.050	1.566
4	VD04	vBWML7	0.535	0.075	1.563
4	dBWML4	hmc	0.721	0.000	1.571
4	dBWMR11	hmc	0.913	0.125	1.558
4	vBWML11	hmc	0.705	0.275	1.543
4	vBWMR11	hmc	0.773	0.325	1.538
3	PHCR	VD12	0.567	3.875	1.173
3	OLQDL	IL1DR	0.757	0.050	1.566
3	IL1DR	URAVR	0.708	0.225	1.548
3	IL1L	IL1R	0.859	0.225	1.548
3	IL1L	URAVR	0.871	0.225	1.548
3	ALA	dBWML7	0.866	0.850	1.486
3	ALA	dBWML8	0.867	0.850	1.486
3	ALA	vBWML8	0.507	0.800	1.491
3	AVFL	AS03	0.625	1.000	1.471
3	dBWML5	hmc	0.806	0.000	1.571
3	dBWMR1	hmc	0.869	2.000	1.369
3	vBWML3	hmc	0.604	0.325	1.538
3	vBWML10	hmc	0.797	0.225	1.548

Distance	Cell names in the pair		Max(T(E))	E(ka)	ka
3	vBWMR10	hmc	0.791	0.325	1.538
3	um1AL	vm2PR	0.659	2.025	1.367
3	um1AR	vm2PL	0.659	2.025	1.367
3	um1PL	vm2AR	0.659	2.025	1.367
3	um1PR	vm2AL	0.659	2.025	1.367
2	pm5VL	mc1V	0.665	2.450	1.323
2	ASEL	AIZL	0.839	2.450	1.323
2	ASKR	PVQL	0.746	3.625	1.200
2	PLNR	PDB	0.802	3.000	1.266
2	PVDL	dBWML7	0.946	0.850	1.486
2	PVDL	dBWML8	0.947	0.850	1.486
2	PVDL	CANR	0.851	0.750	1.496
2	PVDR	dBWML7	0.737	0.850	1.486
2	PVDR	dBWML8	0.738	0.850	1.486
2	PVDR	CANL	0.895	0.750	1.496
2	PHAL	DA09	0.546	3.000	1.266
2	PHAL	PDB	0.662	3.000	1.266
2	PHCL	PDB	0.577	3.000	1.266
2	IL1DR	IL1L	0.781	0.225	1.548
2	IL1DR	IL1VR	0.844	1.425	1.428
2	IL1L	IL1VR	0.511	0.225	1.548
2	IL1R	IL1VL	0.824	0.225	1.548
2	IL1R	URAVR	0.872	0.225	1.548
2	IL1VL	URAVR	0.632	0.225	1.548
2	ALA	hmc	0.560	3.375	1.227
2	PVR	VD12	0.574	3.875	1.173
2	DVB	VA12	0.590	3.875	1.173
2	DVB	VD12	0.734	3.875	1.173
2	AVL	VA12	0.538	3.875	1.173
2	RMEL	RMED	0.949	2.650	1.303
2	RMED	dBWMR1	0.501	2.650	1.303
2	DA09	PDB	0.592	3.000	1.266
2	PDA	VA12	0.586	3.875	1.173
2	PDA	VD12	0.766	3.875	1.173
2	PDB	VD12	0.596	3.875	1.173
2	VB05	VB07	0.628	0.050	1.566
2	vBWML4	hmc	0.803	0.325	1.538
2	vBWML6	hmc	0.822	0.325	1.538
2	vBWMR4	hmc	0.793	0.325	1.538
2	vBWMR6	hmc	0.992	1.800	1.390
2	dBWMR9	hmc	0.807	0.125	1.558
2	vBWML8	exc_gl	0.715	0.800	1.491
2	vBWML9	hmc	0.707	0.225	1.548
2	GLRL	GLRR	0.916	2.650	1.303
2	CANL	CANR	0.999	1.950	1.375
2	mu_anal	mu_sph	0.984	0.050	1.566
2	vm2AL	vm2PL	0.892	1.700	1.400
2	vm2AL	vm2PR	0.888	1.700	1.400
2	vm2AR	vm2PL	0.888	1.700	1.400

Distance	Cell names in the pair		Max(T(E))	E(ka)	ka
2	vm2AR	vm2PR	0.892	1.700	1.400
1	ASEL	AFDL	0.794	0.125	1.558
1	PVDL	PVDR	0.858	0.750	1.496
1	PVDL	ALA	0.704	0.850	1.486
1	PVDL	CANL	0.776	0.750	1.496
1	PVDR	ALA	0.728	0.750	1.496
1	PVDR	CANR	0.914	0.750	1.496
1	PVDR	hmc	0.627	3.475	1.216
1	PHBL	PHBR	0.852	0.375	1.533
1	CEPDL	OLQDL	0.639	0.050	1.566
1	IL1DR	IL1R	0.642	0.225	1.548
1	IL1L	IL1VL	0.599	0.225	1.548
1	IL1R	IL1VR	0.750	0.225	1.548
1	IL1VL	IL1VR	0.973	0.225	1.548
1	IL1VR	URAVR	0.556	0.225	1.548
1	AIZL	AIZR	0.534	0.375	1.533
1	ALA	CANR	0.594	0.750	1.496
1	PVPL	DVC	0.568	0.475	1.523
1	DVB	DD06	0.535	3.750	1.186
1	RIGL	RIGR	0.760	0.925	1.478
1	AVKR	SMBDR	0.895	0.200	1.551
1	PVT	VD12	0.641	3.875	1.173
1	RIVL	RIVR	0.807	0.575	1.513
1	VA12	VD12	0.786	3.875	1.173
1	VB05	VB06	0.950	0.050	1.566
1	dBWMR1	GLRDL	0.884	2.000	1.369
1	dBWMR1	GLRDR	0.752	2.000	1.369
1	vBWML5	hmc	0.790	0.325	1.538
1	vBWML7	hmc	0.662	0.325	1.538
1	vBWMR5	hmc	0.838	0.325	1.538
1	vBWMR7	hmc	0.573	0.325	1.538
1	dBWMR8	hmc	0.946	0.125	1.558
1	vBWML8	hmc	0.774	0.225	1.548
1	CANL	exc_cell	0.762	0.250	1.546
1	CANR	exc_cell	0.761	0.250	1.546
1	mu_intL	mu_intR	0.607	0.050	1.566
1	mu_intL	mu_anal	0.984	0.050	1.566
1	mu_intL	mu_sph	0.984	0.050	1.566
1	mu_intR	mu_anal	0.625	0.050	1.566
1	mu_intR	mu_sph	0.625	0.050	1.566
1	um1AL	um1PL	0.573	2.025	1.367
1	um1AR	um1PR	0.573	2.025	1.367
1	vm2AL	vm2AR	0.927	1.700	1.400
1	vm1AL	vm1AR	0.714	1.750	1.395
1	vm1AL	vm1PL	0.795	1.750	1.395
1	vm1AR	vm1PR	0.795	1.750	1.395
1	vm1PL	vm1PR	0.714	1.750	1.395
1	vm2PL	vm2PR	0.927	1.700	1.400

Table S4. List of cell-pairs with strong transmission except intra body-wall muscles pairs. The first column represents the shortest distance along the network connecting the two cells of the cell-pair. The second and third columns represent the cell names of the cell-pair, and the color painted on the name box stands for the cell type (Red: Pharynx cells, Orange: Sensory neurons, Yellow: Inter neurons, Green: Motor neurons, Light blue: Body-wall muscles, Purple: Other end organs, Magenta: Sex-specific cells). The fourth, fifth, and sixth columns represent the transmission coefficient, the *E* value, and the wavenumber when the cell-pair shows the strongest transmission in the positive *E* value range, respectively.